DOI: 10.1002/((please add manuscript number))
Article type: Communication

High-Performance Solution-Processed Double-walled Carbon Nanotube Transparent Electrode for Perovskite Solar Cells

Il Jeon, Jungjin Yoon, Unsoo Kim, Changsoo Lee, Rong Xiang, Ahmed Shawky, Jun Xi, Junseop Byeon, Hyuck Mo Lee, Mansoo Choi, Shigeo Maruyama*, and Yutaka Matsuo**

Prof. I. Jeon, Prof. R. Xiang, Dr. A. Shawky, Prof. S. Maruyama, Prof. Y. Matsuo
Department of Mechanical Engineering, School of Engineering, The University of Tokyo, Tokyo 113-8656, Japan

Prof. S. Maruyama
Energy NanoEngineering Laboratory, National Institute of Advanced Industrial Science and Technology (AIST), Tsukuba, 305-8564, Japan

Dr. J. Yoon,
Photo-Electronic Hybrids Research Center, National Agenda Research Division, Korea Institute of Science and Technology (KIST), Seoul 02792, Republic of Korea

U. Kim, J. Byeon, Prof. M. Choi,
Department of Mechanical Engineering, Seoul National University, Seoul 08826, Republic of Korea

U. Kim, Dr. J. Xi, J. Byeon, Prof. M. Choi,
Global Frontier Center for Multiscale Energy Systems, Seoul National University, Seoul 08826, Republic of Korea

C. Lee, Prof. H. M. Lee,
Department of Materials Science and Engineering, KAIST, 291 Daehak-ro, Yuseong-gu, Daejeon, 34141, Republic of Korea

E-mail: mchoi@snu.ac.kr, maruyama@photon.t.u-tokyo.ac.jp, matsuo@photon.t.u-tokyo.ac.jp

Keywords: double-walled nanotubes, solution-processed electrode, transparent electrode, indium-free, perovskite solar cells

Double-walled carbon nanotubes are between single-walled carbon nanotubes and multi-walled carbon nanotubes. They are comparable to single-walled carbon nanotubes with respect to the light optical density, but their mechanical stability and solubility are higher. Exploiting such advantages, we demonstrate solution-processed transparent electrodes using

double-walled carbon nanotubes and their application to perovskite solar cells. Perovskite solar cells which harvest clean and infinite solar power has attracted a lot of attention as a next-generation renewable energy source. However, their eco-friendliness, cost, and flexibility are limited by use of transparent oxide conductors, which are inflexible, difficult to fabricate, and made up of expensive rare metals. Solution-processed double-walled carbon nanotubes can replace conventional transparent electrodes to resolve such issues. Perovskite solar cells using the double-walled carbon nanotube transparent electrodes produce an operating power conversion efficiency of 17.2% without hysteresis. As the first solution-processed electrode-based perovskite solar cells, this work will pave the pathway to the large-size, low-cost, and eco-friendly solar devices.

Over the last 20 years, carbon nanotubes (CNTs) have generated a great deal of excitement among researchers for their applicability in electronics.[1–4] In addition to high conductivity, CNTs films demonstrate high transparency with remarkable mechanical resilience.[5] Accordingly, they have been regarded as a promising alternative to conventional electrodes, such as indium tin oxide (ITO)[6–11] and metals[12–16]. Thus far, single-walled CNTs (SWNTs) have frequently been the subject of study for transparent electrode applications.[17,18] This is because SWNTs possess a lower optical density than multi-walled CNTs (MWNTs). However, MWNTs have a unique advantage of being easily dispersed in solution, which enables solution-processable transparent electrodes. Since other carbon electrodes, such as graphene[19,20] and carbon pastes[21,22], are not solution-processable, capitalizing on this trait could potentially be the game changer in optoelectronics. Double-walled CNTs (DWNTs), which have a two concentric graphitic tubular shape, is structurally intermediate between SWNTs and MWNTs.[23] DWNTs have the best of both worlds in the way that they exhibit good dispersibility and chemical stability of MWNTs while

demonstrating high transparency and conductivity of SWNTs.[24] In other words, for solution-processable CNT electrodes, DWNTs are the perfect candidate. Moreover, DWNTs are chemically[25], mechanically[26], and thermally[27,28] more stable than SWNTs. It is our opinion that DWNTs have been overshadowed by the recent development of SWNTs.

In the wake of an environmentally sustainable society, organometallic halide perovskite solar cells (PSCs) have emerged as a promising thin-film photovoltaic with its high power conversion efficiency (PCE) and solution-processability.[29,30] While high PCE is an eye-catching property at a laboratory level, it is only part of a big picture for industrial applications. In order for PSCs to maximize their potential, it is imperative that their high-cost ITO – or fluorine-doped tin oxide (FTO) – are replaced by a cost-effective alternative, such as CNTs.[31,32] In this regard, demonstrating the applicability of solution-processable DWNT electrode in PSCs can open the door to large-size and low-cost PSCs, bringing a step closer to commercialization.

In this work, we synthesized solution-processed DWNT electrodes, which demonstrate excellent optical conductivity, and demonstrated their applicability as transparent electrodes in PSCs. Narrowly distributed diameters of long DWNTs were synthesized and slot-die coated on large glass substrates.[33] We studied the optical conductivity of the DWNT electrode and characteristics of chemical doping. Owing to the uniform diameters and controlled tube lengths, DWNT films exhibited higher transparency and conductivity than the previously reported CNT electrodes. Furthermore, the DWNT films displayed weaker doping effect upon chemical doping compared with SWNTs, on account of the inner wall of the double-walled structure having less susceptibility to chemicals and the surrounding surfactants protecting the nanotubes. Despite the relatively weaker doping effect, DWNT films showed more uniform morphology and favorable energy alignments than the previously reported SWNT electrodes. Accordingly, the inverted-type PSCs fabricated using the DWNT

films exhibited a PCE of 15.6% before doping, which improved to 16.7% and 17.2% upon HNO_3 and trifluoromethanesulfonic acid (TFMS) doping, respectively.

High conductivity and transparency of DWNTs come from a perfect shell structure and a suitable diameter that suppress light absorption of the polarization components perpendicular to the CNT axis.[34,35] Moreover, the tube length, dispersion states, and weight-ratios of surfactants to DWNTs are the key to obtaining highly conductive DWNTs.[26,36–38] Our DWNT films were prepared according to Imazu *et al.*,[33] which displayed long DWNTs with diameters of 2 – 3 nm with the optimum surfactant/DWNT ratio.[24] Exploiting the solution-processability, DWNT solutions were slot-die coated onto large glass substrates (**Figure S1**). Their conductivity was measured using the van der Pauw method of four probe measurement (**Figure 1a and Table S1**). **Figure 1a** shows the sheet resistance (R_{sheet}) over transmittance at 550 nm wavelength of light of the DWNT films produced in this work compared with the previously reported DWNT electrodes [26,39–41] and SWNT electrodes[17]. The optical conductivity of our solution-processed DWNT films surpass even the floating catalyst-synthesized SWNT films[10]. This is attributed to the fact that the solution-processed DWNTs have larger tube-diameters and more metallic characteristics, being multi-layered. In addition, the fact that the individual tubes are separated by surfactants may reduce Schottky CNT junction contact resistance, thereby improving the conductivity of the entire film.[41] Regardless of the level of optical conductivity, pristine carbon electrodes need to be doped by chemicals to enhance the conductivity. HNO_3 and TFMS are two of the common dopants used for their doping effectiveness, the former being an established dopant and the latter being more contemporary with superior doping durability. **Figure 1b** shows the R_{sheet} decreases in DWNT films upon HNO_3 and TFMS treatments. Unlike SWNT electrodes, the decreases in R_{sheet} were relatively weak compared with the previous observations on other carbon electrodes. R_{sheet} decreased to approximately 84% of that of the pristine DWNTs upon

application of 1 v/v% HNO_3. The doping effect was limited to *ca.* 72.8% even after increasing the concentration of HNO_3 to 10 v/v%. This is in stark contrast to the SWNT's case, in which the R_{sheet} decreased to below one third of that of the pristine SWNTs upon HNO_3 doping[42] and the doping effect gradually increased with the increase in the acid concentration up to *ca.* 35 v/v%,[6] according to our previous studies. Doping effect was stronger when TFMS was applied. R_{sheet} decreased to 57.9% of that of the pristine DWNT films when only a small concentration (2 v/v%) of TFMS was applied. This is in disagreement with our previous study using SWNTs,[11] where both HNO_3 and TFMS manifested a similar level of doping effectiveness. It was interesting that a saturation point of the doping effect of TFMS on DWNTs occurred at a smaller concentration (2 v/v%) compared with the HNO_3 doping case (5 v/v%). In terms of durability, however, DWNTs and SWNTs shared the same outcome of the TFMS doping effect lasting for more than 100 days and the HNO_3 doping effect disappeared after 10 days (**Figure 1c and Table S2**).[11,43] The different behaviors in doping effectiveness between DWNTs and SWNTs can be speculated by looking at the transmission electron microscopy (TEM) images of the DWNT films (**Figure S2a and S2b)**. The TEM images show predominantly double-walled tubes with uniform diameters. Selected area electron diffraction (SAED) supports this with a strong graphite (002) plane ring, indicating a large portion of double walls **(Figure S2c and S2d)**. We can conjecture that the doping effect imposed on the inner walls must be relatively weaker than the outer walls as the acids cannot get inside the inner walls.[44] Furthermore, many of the DWNTs are wrapped around by the surfactants (**Figure 1d**) and only small portions of nanotubes are exposed (**Figure 1d inset**). As the chemical dopants have to sit directly next to the tubes to induce maximum doping effects, these surfactants must inhibit the interaction between the tubes and acids is the reason for the limited doping effect.[43] We studied these points in more detail by calculating the binding energy between DWNTs and the doping acids using the density functional theory (DFT) (**Figure 1e and 1f**). Since CNTs can have semiconducting and conducting properties

depending on their chirality, we used zigzag DWNTs and armchair DWNTs to simulate semiconducting DWNTs (**Figure 1e**) and metallic DWNTs (**Figure 1f**) respectively. TFMS resulted in much stronger binding energy on DWNTs (~0.25 eV on zigzag DWNTs and ~0.33 eV on armchair DWNTs) than HNO_3 (~0.09 eV on zigzag DWNTs and ~0.12 eV on armchair DWNTs), which agrees with the empirical data (**Figure 1e, 1f, and S3**). It was interesting to observe both TFMS and HNO_3 exhibiting greater doping on the metallic armchair DWNTs than semiconducting zigzag DWNTs. We calculated the charge transfer between the dopants and DWNTs using the Bader charge analysis to observe the doping effects on the outer walls and inner walls of DWNTs (**Table 1 and S3**). **Table 1** shows that the electrons transfer occurs dominantly from the outer walls of DWNT to the dopants than from the inner walls. This explains why intrinsically strong dopants, such as TFMS, are necessary to effectively dope DWNTs, because strong dopants can induce charge transfer even from the inner walls. The calculated electron transfer from DWNTs to acids decreased as the distance of dopant from DWNTs increased in both the HNO_3 and TFMS cases (**Figure S4**). The doping effect reached almost zero when the distance was 4 Å. This means that the surfactants surrounding the DWNTs completely hinder the doping effect and only exposed DWNTs can undergo doping.

The nature of our DWNTs samples and the related doping effects can be better understood using Raman spectroscopy and near-infrared absorption spectroscopy. Fundamentally, DWNTs adopt four distinct permutations depending on the metallic or semiconducting properties in the inner and outer walls (**Figure 2a**). Using the resonance of DWNTs with different laser lines, we can analyze the inner walls and outer walls of DWNTs separately. For the DWNTs with metallic inner walls and semiconducting outer walls, a G-band appears as a G^+ peak above 1590 cm^{-1} and a G^- peak below <1590 cm^{-1} under the 532 nm laser line (**Figure 2b**).[45] The G^+ peak corresponds to carbon atom vibrations along the CNT axis, whereas the G^- peak is associated with the vibrations in a circumferential direction.[46] In our measurement, the upshifts of the G^- peak were more prominent than those

of the G^+ peak upon both HNO_3 and TFMS doping. It was clear that the G peak of the TFMS-doped DWNTs shifted to a higher frequency than those of the pristine and HNO_3-doped DWNTs. It is reported that the 2D peaks appear separated under the strong 532 nm laser line.[47] The inner walls of DWNTs are associated with the 2D-band at a low frequency while the outer walls are associated with the 2D frequency at a high frequency.[45] For the HNO_3-doped DWNTs, only the 2D peak at a higher frequency shifted (**Figure 2b inset**). However, for the TFMS-doped DWNTs, both of the 2D peaks shifted. This corroborates our finding from the DFT calculation that the stronger dopant, TFMS induces a greater doping effect, because it dopes the inner walls as well as the outer walls. The 785 nm laser line is said to excite G-band of the metallic outer-walls and semiconducting inner-walls.[45] We can observe that the G-band of both HNO_3-doped DWNTs and TFMS-doped DWNTs shifted to a higher frequency, indicating a doping effect (**Figure 2c**). However, the differences in the shifts were marginal, which can be ascribed to the lower laser power, rather than lack of doping effect. The visible and near-infrared absorbance (Vis-NIR) spectra of the undoped DWNT films indicates the M_{11} transition for both inner and outer walls, and the S_{11} transition for the inner walls (**Figure 2d**).[48,49] S_{11} excitation of the outer walls could not be observed, insinuating that our DWNT films may contain a very small amount of semiconducting outer walls. This is quite clear as the S_{11} transition of the outer wall does not overlap with other peaks, such as water, which has absorption at a similar wavelength range. On the other hand, the analysis of the inner wall is rather complicated as the peaks of the inner walls and outer walls of both the M_{11} and S transitions overlap. When HNO_3 was applied, the semiconducting S transitions decreased substantially, and the metallic M_{11} transition peak decreased slightly. Intriguingly, When TFMS was applied, both the M_{11} and S peaks were subdued further with the reduction of the M_{11} peak being slightly stronger than the S peak. In addition, the absorption spectra show that the transitions of the outer walls reduced more than those of the inner walls upon doping which is what we would expect from the DFT calculations and Raman spectroscopy

data.[50] By reading the radial breathing mode (RBM) of Raman spectroscopy, we can probe the semiconducting and metallic tubes of inner walls and outer walls separately.[45] The resonance of the inner walls can be observed above 200 cm^{-1} while that of the outer walls can be observed below 200 cm^{-1}.[51,52] The RBM spectra transitions were assigned based on the Kataura plot.[53,54] Under both the 532 nm and 785 nm laser lines, the intensity of the transitions is reported to decrease when DWNTs are doped and the peaks are shifted to a higher frequency.[55] It is evident that the intensities of both HNO_3- and TFMS-doped DWNTs decreased substantially. The reduction is greater for the TFMS treatment than the HNO_3 treatment as expected. The intensity reduction alone cannot indicate the doping, because the disappearance of small CNTs by protonation and existence of impurities, such as surfactants, can lower the Raman intensity at the RBM region as well.[56,57] Therefore, the peak shifts should also be considered for the confirmation of the doping effect.[58] **Figure 2e** shows that metallic peaks of inner walls shifted to higher frequencies under both HNO_3 and TFMS doping by similar wavenumbers, which is little different from what was observed in 2D-band shifts (**Figure 2b inset**). In the case of semiconducting peaks of the outer walls, there was no shift even though the peak came from the outer walls. This may prove the finding from the Vis-NIR data that there are no semiconducting outer walls in our DWNT films. **Figure 2f** shows that there was no shift of semiconducting peak of the inner walls, which means there was possibly no or extremely weak doping effect. This is understandable as the peak corresponds to semiconducting inner walls, which were found to be much harder to dope relative to metallic and outer wall counterparts. The metallic transition has two peaks, which is typical for DWNTs.[59] It has been reported that the peak at 175 cm^{-1} is supposed to shift to a higher frequency upon functionalization.[59,60] This peak shifts the most for the TFMS-doped DWNT film, proving that the metallic outer walls experience a greater doping effect by TFMS than HNO_3.

Inverted type planar PSCs were fabricated using the slot-die coated DWNT as the transparent electrode (**Figure 3a**). The device configuration was DWNT/poly(triaryl amine) (PTAA) [35 nm] /$MA_{0.6}FA_{0.4}PbI_{2.9}Br_{0.1}$ [450 nm] /C_{60} [20nm] / bathocuproine (BCP) [6 nm] /Cu [50 nm] as it can be seen from the cross-sectional scanning electron microscope (SEM) image (**Figure 3b**). PTAA percolated into the network of DWNTs thoroughly and the combined thickness was approximately 35 nm. The transparent electrodes, we tested, were pristine DWNTs, HNO_3-doped DWNTs, TFMS-doped DWNTs, and ITO. **Table 2** shows the pristine DWNT-based PSCs exhibiting a PCE of 15.6%. The PCE improves to 16.7% and 17.2% upon HNO_3 and TFMS doping, respectively (**Figure 3c and Table 2**). The improvement comes mainly from the substantially increased fill factor (FF) and slightly enhanced open circuit voltage (V_{OC}). The V_{OC} increased because of a better energy alignment between DWNT and PTAA after doping (**Figure 3d**). Photoelectron yield spectroscopy (PYS) data show that DWNT films possess a Fermi level of –5.0 eV, which is a typical value for carbon electrodes (**Figure S5**).[6,10,12,13,17,42,61–64] The Fermi level decreased to *ca.* –5.2 eV upon HNO_3 and TFMS doping, which aligned well with the highest occupied molecular orbitals (HOMOs) of PTAA (–5.2 eV). In fact, the limited doping effect of DWNT led to a better energy alignment than the SWNT electrodes, which translate to higher V_{OC}. Previously reported SWNT transparent electrode-based solar cells suffer from lower V_{OC} compared with the ITO-based references, which we suspect arises from the energy mismatch ascribed to the low-lying Fermi levels of doped-SWNTs (**Figure S5 and Table S4**).[6,7,10,11,17,42] However, our acid doped-DWNT-based PSCs exhibited V_{OC} almost the same as that of the ITO-based devices (**Table S5 and Figure S6**). Not only the energy level alignment but also morphology of the electrode and the charge-selective layer is linked to V_{OC}.[65] **Figure 4** shows atomic force microscope (AFM) images and root mean square average (RMS) roughness values of the DWNT films with and without PTAA coating. The data show that our DWNT films have

much smoother morphology compared with the reported aerosol-synthesized SWNT films (**Figure S7**).[6,7,10,11,17,42] It can be attributed to the solution-processed DWNTs containing surfactants within the DWNT network. It is important to note that PTAA coating reduced the roughness significantly and the roughness of our DWNT after PTAA deposition is comparable to those of even graphene and ITO.[7,19,20] This led to the morphology of the perovskite films spin-coated on top possessing similar quality among the samples (**Figure S8**). We think that both the excellent morphology of the DWNT electrodes and energy level alignment resulted in the high V_{OC}. The improvement of FF for the acid doped-DWNT-based PSCs is easy to understand as the doping effect should lower the series resistance (R_S) of DWNT-based PSCs, which in turn increases FF (**Figure 5a and S9**). It is worth noting that the difference in R_{sheet} did not influence R_S as greatly as we anticipated, which, we surmise, is because of the lab scale fabrication of the solar devices. Instead, shunt resistance (R_{SH}) contributed to the FF increase significantly (**Figure 5b**). The TFMS-based PSCs exhibited higher R_{SH} than the HNO_3-based PSCs. We conducted steady-state photoluminescence (PL) and time-resolved PL (TRPL) to understand the origin of the R_{SH} difference. Steady-state PL shows that the quenching of the perovskite film on the acid-doped DWNT films is much greater than that of the perovskite film on the pristine DWNT film (**Figure 5c**). Nevertheless, the quenching difference between the HNO_3-doped DWNT film and TFMS-doped DWNT film was marginal as reflected by the similar V_{OC} values, which probably is due to the similar Fermi levels of the HNO_3-doped DWNT film and TFMS-doped DWNT film. TRPL data are congruent with the steady-state PL (**Figure S10**). Discovering that the difference in charge-extraction dynamics between HNO_3-doped DWNTs and TFMS-doped DWNTs is the same from the PL measurements, we analyzed the dark *J–V* curves of the devices to investigate the unwanted current path.[66–68] **Figure 5d** reveals that the dark *J–V* curve of the acid-doped DWNT-based PSCs have one to two orders lower leakage current than the pristine DWNT-based PSCs. In addition, the TFMS-doped DWNT-based PSCs have an even less leakage

current than the HNO_3-doped DWNT-based PSCs. This implies reduced non-radiative recombination in the TFMS-doped DWNT-based PSCs, explaining the higher R_{SH} value. Furthermore, the threshold voltage of the TFMS-doped DWNT-based PSCs was approximately 1.0 V, which points to a better charge-injection barrier than the HNO_3-doped DWNT-based PSCs, as evidenced by slightly higher short-circuit current (J_{SC}) values compared with those of the HNO_3-doped DWNT-based PSCs.[69] In fact, the dark *J–V* curve of the ITO-based PSCs exhibits a similarly low threshold voltage to that of the TFMS-doped DWNT-based PSCs (**Figure S11**). However, the J_{SC} of the ITO-based PSCs (22.9 mA cm^{-2}) was marginally higher than that of the TFMS-doped DWNT-based PSCs (21.4 mA cm^{-2}). This is because of the difference in the optical transmittance of the films (**Figure S12a**). The absorption spectra show that the perovskite films on ITO absorb more light at around 480 nm (**Figure S12b**). Such optical characteristics were displayed in external quantum efficiency (EQE) spectra in which integrated J_{SC} were found to be 20.7 and 21.4 mA cm^{-2} for the DWNT- and ITO-based PSCs (**Figure S12c**). Overall, despite the slightly lower PCE than the ITO-based devices, the TFMS-doped DWNT-based PSCs have the upper hand in solution-processability, lower fabrication cost, and natural abundance. In addition, the TFMS-doped DWNT-based PSCs does not show hysteresis (**Figure S13** and **Table S6**) and their maximum power point tracking PCE shows a stable 17.2% of operating efficiency (**Figure 5e**). The reproducibility was also high for the acid-doped DWNT-based PSCs compared to the pristine DWNT-based PSCs (**Figure S14**). The DWNT-based PSCs displayed similar stability as the ITO-based PSCs. Yet, the TFMS-doped DWNT-based PSCs showed a marginally lower stability compared with the other devices (**Figure S15a**). We suspect that this might be due to the hygroscopic nature of TFMS. The stability test conducted under a severe condition (50 °C, 90% humidity) shows that there is no significant difference in device stability, supporting our surmise (**Figure S15b**). The obtained PCE was compared with the reported performance of other transparent conductive oxide (TCO)-free PSCs. We included CNT-based electrodes as

well as silver nanowire (AgNW), because AgNW is known as the high-performance solution-processable electrodes. The PCE obtained in this work stands the highest among the reported transparent conductive oxide (TCO)-free PSCs employing CNTs and solution-processed AgNW as a bottom electrode (**Figure S16** and **Table S7**). It is the highest when we take all of the reported CNT electrode-based PSCs, even for the top electrode if we consider stabilized PCEs, to the best of our knowledge (**Figure 5f** and **Table S8**). It is worth mentioning that this work is both the first demonstration of DWNTs as a transparent electrode and the first solution-processed CNT electrode in PSCs.

In conclusion, we showcased the application of solution-processed DWNTs as transparent electrodes in PSCs. It was apparent that TFMS exhibited a stronger doping effect than HNO_3 on DWNTs. The doping behavior in DWNTs was rather different from what would be expected in SWNTs; the observed doping effect was much milder in DWNTs relative to the previously reported SWNTs. This was because most DWNTs were protected by surfactants and the inner walls of DWNTs were difficult to be doped by the acids. Nonetheless, such limited doping effect favored the energy level alignment with the PTAA and perovskite layers that they displayed excellent charge extraction properties as evidenced by the high V_{OC}. In addition, The fact that DWNTs possess improved lifetime and current densities for field emission,[70] and the smoother morphology of DWNT films compared with the previously reported SWNTs contributed to high device performance too. A PCE of 17.2% was obtained from the TFMS-doped DWNT-based PSCs, which is the record-high efficiency among the reported CNT- and AgNW-based TCO-free PSCs and the reported CNT electrode-based PSCs.

Experimental Section

DWNT Synthesis: DWNTs were grown by a catalytic high-temperature chemical vapor deposition. DWNTs were dispersed using a tip-type sonicator (Ieda Trading Corporation, VCX-130) for 45 min at 20 W at carboxyl methyl cellulose sodium salt (Sigma-Aldrich) /DWNTs = 6 (w/w%), then ultra-centrifugated (Hitachi Koki, himac, CP-WX) at 147000 g for 8 h. The top-80% portion of the supernatant was collected, and the sediment was redispersed in water. The sediment/water = 0.04 (w/w%). The DWNT dispersion was diluted in water to 0.04 wt%, which was slot-die coated on large glass substrates, followed by heating at 125 °C for 1 min. The DWNT-coated substrates were submerged in ethanol for 24 h to remove impurities and surfactants.

Device Fabrication: The DWNT substrates were cut to smaller substrates for the fabrication at a lab scale (25 × 25 mm^2). For the HNO_3 doping, 100 μL of HNO_3 (70% concentration, Sigma Aldrich) diluted in deionized water (30% v/v) was spin-coated onto the DWNT/glass substrates at 4000 rpm for 60 s, followed by drying under 80 °C for 30 min and 100 °C for 10 min. In the case of TFMS doping, 100 μL of TFMS solution diluted in chlorobenzene (8% v/v) was spin-coated at 4000 rpm for 60 s and the substrate was dried under 130 °C for 30 min. For the ITO substrates, pre-patterned ITO/glass substrates (12 ohm $sq.^{-1}$, 25 × 25 mm^2) (AMG Tech) were cleaned through sonication in acetone, isopropyl alcohol, and deionized water for 15 min, respectively, and stored in a drying oven at a temperature of 120 °C for 20 min. PTAA solution was prepared by dissolving 8 mg of PTAA (Sigma Aldrich) in 1 mL of 2,3,5,6-tetrafluoro-7,7,8,8-tetracyanoquinodimethane (F4 TCNQ)-added solution which was prepared by dissolving F4 TCNQ into chlorobenzene (Sigma Aldrich) in a concentration of 1 wt%.[71] Then, the PTAA layer was formed by spin-coating the solution on the DWNT (or ITO) substrates with 4000 rpm for 30 s and then annealed on a hotplate at a temperature of

100 °C for 10 min. To secure a reproducible coating of perovskite film on the hydrophobic PTAA layer, poly[(9,9-bis(30-((N,N-dimethyl)-N-ethylammonium)-propyl)-2,7-fluorene)-alt-2,7-(9,9-dioctylfluorene)] dibromide (PFN-P2) (1-Material) was introduced as an interfacial compatibilizer.[72] Its precursor solution was prepared by dissolving PFN-P2 in methanol with a concentration of 0.4 mg mL^{-1} and spin-coated on the PTAA layer at 4000 rpm for 20 s. Perovskite layer with a composition of $MA_{0.6}FA_{0.4}PbI_{2.9}Br_{0.1}$ was fabricated using a reported method[73]. Perovskite precursor solution was prepared by dissolving 461 mg of PbI_2 (Tokyo Chemical Industry), 79.5 mg of methylammonium iodide (MAI) (Greatcell Solar), 68.8 mg of formamidinium iodide (FAI) (Greatcell Solar), 11.2 mg of methylammonium bromide (MABr) (Greatcell Solar) and 75 μL of the urea-added dimethylsulfoxide (DMSO) (Sigma Aldrich) in 0.55 mL of *N*-dimethylformamide (DMF) (Sigma Aldrich). The urea solution was prepared by dissolving urea (Sigma Aldrich) in DMSO at a concentration of 44.4 mg mL^{-1} to induce large grain crystallization of perovskite film.[74] The perovskite precursor solution was stirred for 1 hour under room temperature. The solution was spin-coated at 4000 rpm for 20 s. 3~500 μL of diethyl ether antisolvent was applied 7 s after the beginning of the spin-coating. A transparent film of perovskite intermediate phase was formed and changed into a black perovskite film after annealing under a temperature of 130 °C for 20 min. The whole spin-coating process was conducted under the controlled temperature (25 °C) and relative humidity (<10%). Then, C_{60} (20 nm) and BCP (6 nm) layers were deposited through a square metal mask of 1.5 × 1.5 cm^2 and Cu electrode was deposited to complete devices with an area of 0.15 × 0.60 cm^2 (0.090 cm^2) under a pressure of $<5.0 \times 10^{-6}$ torr inside a thermal evaporator.

Material and Device Characterization: *J–V* curves of perovskite solar cells under light were measured using a source meter (Keithley 2400, Tektronix) at a step voltage of 20 mV and a delay time of 50 ms for both the forward and reverse scan directions. A metal aperture mask having an area of 0.13 × 0.58 cm^2 (0.0754 cm^2) was used during the *J-V* measurement. AM

1.5G illumination was simulated using a solar simulator (Solar 3A Class, Oriel) with a KG-5-filtered silicon standard cell. *J–V* curves under dark condition were measured using a probe station built inside a dark-shield box. SEM measurement was conducted using field-emission scanning electron microscopy (Auriga, Carl Zeiss). Optical transmittance and absorption spectra were obtained using a UV-vis-NIR spectrophotometer (Cary 5000, Agilent Technologies). Time-resolved and steady-state PL measurement were carried out using a spectrofluorometer (FluoroMax-4, Horiba) with a 463-nm laser diode (DeltaDiode-470L, Horiba). Surface topography measurement was conducted using an atomic force microscope (NX10, Park Systems) via non-contact mode. EQE spectra were obtained using a quantum efficiency system (IQE-200B, Oriel) with a chopper frequency of 100 Hz. The van der Pauw method of four probe measurement was conducted using a probe station and indium metal pieces. For the theoretical study, GGA-level spin-polarized DFT calculation was performed as implemented in Vienna ab initio simulation (VASP) package code with a plane wave basis-set. The exchange-correlation energy was described with the Perdew-Burke-Ernzerhof (PBE)[75] functional. The Brillouin zone was sampled with a 1 × 1 × 2 k-point mesh following the Monkhorst−Pack scheme. The convergence criteria for electronic and geometric optimization were 10^{-4} eV and 0.01 eV $Å^{-1}$, respectively. The cut-off energy was set to 400 eV. The structure configurations of DWNTs were constructed as described in the previous study[76]. The isolated DWNT were geometrically optimized through fully relaxing the atomic structure. Bader charge analysis[77] was performed for the charge transfer between the dopants and DWNTs.

Supporting Information

Supporting Information is available from the Wiley Online Library or from the author.

Acknowledgements

I.J., J.Y., and U.K. contributed equally to this work. We gratefully acknowledge the Researchand Education Consortium for Innovation of Advanced Integrated Science by Japan Science and Technology (JST) and Japan Society for the Promotion of Science (JSPS) KAKENHIGrant Numbers JP15H05760, JP16H02285, JP17H06609, and JP19K15669. I.J. thanks Yashima foundation for financial support. This work has been supported by the Global Frontier R&D Program of the Center for Multiscale Energy Systems funded by the National Research Foundation under the Ministry of Science and ICT, Korea (2012M3A6A7054855).

Received: ((will be filled in by the editorial staff))
Revised: ((will be filled in by the editorial staff))
Published online: ((will be filled in by the editorial staff))

References

[1] S. Iijima, T. Ichihashi, *Nature* **1993**, *363*, 603.
[2] K. S. Ibrahim, *Carbon Lett.* **2013**, *14*, 131.
[3] S. Park, M. Vosguerichian, Z. Bao, *Nanoscale* **2013**, *5*, 1727.
[4] W. D. H. RH Baughman, AA Zakhidov, *Science* **2002**, *297*, 787.
[5] S. Iijima, C. Brabec, A. Maiti, J. Bernholc, *J. Chem. Phys.* **1996**, *104*, 2089.
[6] I. Jeon, T. Chiba, C. Delacou, Y. Guo, A. Kaskela, O. Reynaud, E. I. Kauppinen, S. Maruyama, Y. Matsuo, *Nano Lett.* **2015**, *15*, 6665.
[7] I. Jeon, J. Yoon, N. Ahn, M. Atwa, C. Delacou, A. Anisimov, E. I. Kauppinen, M. Choi, S. Maruyama, Y. Matsuo, *J. Phys. Chem. Lett.* **2017**, *8*, 5395.
[8] S. N. Habisreutinger, R. J. Nicholas, H. J. Snaith, *Adv. Energy Mater.* **2017**, *7*, 1601839.
[9] C. Delacou, I. Jeon, S. Seo, T. Nakagawa, E. I. Kauppinen, S. Maruyama, Y. Matsuo, *ECS J. Solid State Sci. Technol.* **2017**, *6*, M3181.
[10] I. Jeon, K. Cui, T. Chiba, A. Anisimov, A. G. Nasibulin, E. I. Kauppinen, S. Maruyama, Y. Matsuo, *J. Am. Chem. Soc.* **2015**, *137*, 7982.
[11] I. Jeon, C. Delacou, H. Okada, G. E. Morse, T.-H. Han, Y. Sato, A. Anisimov, K. Suenaga, E. I. Kauppinen, S. Maruyama, Y. Matsuo, *J. Mater. Chem. A* **2018**, *6*, 14553.
[12] J.-W. Lee, I. Jeon, H.-S. Lin, S. Seo, T.-H. Han, A. Anisimov, E. I. Kauppinen, Y. Matsuo, S. Maruyama, Y. Yang, *Nano Lett.* **2018**, acs. nanolett.8b04190.
[13] N. Ahn, I. Jeon, J. Yoon, E. I. Kauppinen, Y. Matsuo, S. Maruyama, M. Choi, *J. Mater. Chem. A* **2018**, *6*, 1382.
[14] T. Sakaguchi, I. Jeon, T. Chiba, A. Shawky, R. Xiang, S. Chiashi, E. I. Kauppinen, N.-G. Park, Y. Matsuo, S. Maruyama, *MRS Commun.* **2018**, *8*, 1058.
[15] K. Aitola, K. Sveinbjörnsson, J.-P. Correa-Baena, A. Kaskela, A. Abate, Y. Tian, E. M. J. Johansson, M. Grätzel, E. I. Kauppinen, A. Hagfeldt, G. Boschloo, *Energy Environ. Sci.* **2016**, *9*, 461.
[16] K. Aitola, K. Domanski, J.-P. Correa-Baena, K. Sveinbjörnsson, M. Saliba, A. Abate, M. Grätzel, E. Kauppinen, E. M. J. Johansson, W. Tress, A. Hagfeldt, G. Boschloo, *Adv. Mater.* **2017**, *29*, 1606398.
[17] I. Jeon, Y. Matsuo, S. Maruyama, *Top. Curr. Chem.* **2018**, *376*, 4.
[18] I. Jeon, R. Xiang, A. Shawky, Y. Matsuo, S. Maruyama, *Adv. Energy Mater.* **2018**,

1801312, 1801312.
[19] H. Sung, N. Ahn, M. S. Jang, J. Lee, H. Yoon, N. Park, M. Choi, *Adv. Energy Mater.* **2016**, *6*, 1501873.
[20] J. Yoon, H. Sung, G. Lee, W. Cho, N. Ahn, H. S. Jung, M. Choi, *Energy Environ. Sci.* **2017**, *10*, 337.
[21] Y. Rong, Y. Hu, A. Mei, H. Tan, M. I. Saidaminov, S. Il Seok, M. D. McGehee, E. H. Sargent, H. Han, *Science* **2018**, *361*, eaat8235.
[22] H. Chen, S. Yang, *Adv. Mater.* **2017**, 1603994.
[23] M. Endo, H. Muramatsu, T. Hayashi, Y. A. Kim, M. Terrones, M. S. Dresselhaus, *Nature* **2005**, *433*, 476.
[24] Z. Li, H. R. Kandel, E. Dervishi, V. Saini, A. S. Biris, A. R. Biris, D. Lupu, *Appl. Phys. Lett.* **2007**, *91*, 053115.
[25] A. H. Brozena, J. Moskowitz, B. Shao, S. Deng, H. Liao, K. J. Gaskell, Y. Wang, *J. Am. Chem. Soc.* **2010**, *132*, 3932.
[26] A. A. Green, M. C. Hersam, *Nat. Nanotechnol.* **2009**, *4*, 64.
[27] T. Sugai, H. Yoshida, T. Shimada, T. Okazaki, H. Shinohara, *Nano Lett.* **2003**, *3*, 769.
[28] Y. A. Kim, H. Muramatsu, T. Hayashi, M. Endo, M. Terrones, M. S. Dresselhaus, *Chem. Phys. Lett.* **2004**, *398*, 87.
[29] J. Xi, K. Xi, A. Sadhanala, K. H. L. Zhang, G. Li, H. Dong, T. Lei, F. Yuan, C. Ran, B. Jiao, P. R. Coxon, C. J. Harris, X. Hou, R. V. Kumar, Z. Wu, *Nano Energy* **2019**, *56*, 741.
[30] H. Dong, J. Xi, L. Zuo, J. Li, Y. Yang, D. Wang, Y. Yu, L. Ma, C. Ran, W. Gao, B. Jiao, J. Xu, T. Lei, F. Wei, F. Yuan, L. Zhang, Y. Shi, X. Hou, Z. Wu, *Adv. Funct. Mater.* **2019**, 1808119.
[31] A. Kumar, C. Zhou, *ACS Nano* **2010**, *4*, 11.
[32] S.-H. Bae, H. Zhao, Y.-T. Hsieh, L. Zuo, N. De Marco, Y. S. Rim, G. Li, Y. Yang, *Chem* **2016**, *1*, 197.
[33] N. Imazu, T. Fujigaya, N. Nakashima, *Sci. Technol. Adv. Mater.* **2014**, *15*, 025005.
[34] R. A. Z, Wu, Chen Z, Du X, Logan JM, Sippel J, Nikolou M, Kamaras K, Reynolds JR, Tanner DB, Hebard AF, *Science* **2004**, *305*, 1273.
[35] Y. Zhou, S. Shimada, T. Saito, R. Azumi, *J. Appl. Phys.* **2015**, *118*, 215305.
[36] A. Kaskela, A. G. Nasibulin, M. Y. Timmermans, B. Aitchison, A. Papadimitratos, Y. Tian, Z. Zhu, H. Jiang, D. P. Brown, A. Zakhidov, E. I. Kauppinen, *Nano Lett.* **2010**, *10*, 4349.
[37] S. Ohmori, T. Saito, B. Shukla, M. Yumura, S. Iijima, *ACS Nano* **2010**, *4*, 3606.
[38] D. Chattopadhyay, S. Lastella, S. Kim, F. Papadimitrakopoulos, *J. Am. Chem. Soc.* **2002**, *124*, 728.
[39] Y. T. Park, A. Y. Ham, Y.-H. Yang, J. C. Grunlan, *RSC Adv.* **2011**, *1*, 662.
[40] G.-H. Xu, J.-Q. Huang, Q. Zhang, M.-Q. Zhao, F. Wei, *Appl. Phys. A* **2011**, *103*, 403.
[41] P.-X. Hou, B. Yu, Y. Su, C. Shi, L.-L. Zhang, C. Liu, S. Li, J.-H. Du, H.-M. Cheng, *J. Mater. Chem. A* **2014**, *2*, 1159.
[42] I. Jeon, S. Seo, Y. Sato, C. Delacou, A. Anisimov, K. Suenaga, E. I. Kauppinen, S. Maruyama, Y. Matsuo, *J. Phys. Chem. C* **2017**, *121*, 25743.
[43] T.-H. Han, S.-J. Kwon, N. Li, H.-K. Seo, W. Xu, K. S. Kim, T.-W. Lee, *Angew. Chemie Int. Ed.* **2016**, *55*, 6197.
[44] J. Miyamoto, Y. Hattori, D. Noguchi, H. Tanaka, T. Ohba, S. Utsumi, H. Kanoh, Y. A. Kim, H. Muramatsu, T. Hayashi, M. Endo, K. Kaneko, *J. Am. Chem. Soc.* **2006**, *128*, 12636.
[45] F. Villalpando-Paez, H. Son, S. G. Chou, G. G. Samsonidze, Y. A. Kim, H. Muramatsu, T. Hayashi, M. Endo, M. Terrones, M. S. Dresselhaus, *Phys. Rev. B* **2009**, *80*, 035419.
[46] M. S. Dresselhaus, G. Dresselhaus, R. Saito, A. Jorio, *Phys. Rep.* **2005**, *409*, 47.

[47] A. Morelos-Gómez, M. Fujishige, S. Magdalena Vega-Díaz, I. Ito, T. Fukuyo, R. Cruz-Silva, F. Tristán-López, K. Fujisawa, T. Fujimori, R. Futamura, K. Kaneko, K. Takeuchi, T. Hayashi, Y. A. Kim, M. Terrones, M. Endo, M. S. Dresselhaus, *J. Mater. Chem. A* **2016**, *4*, 74.
[48] A. A. Green, M. C. Hersam, *ACS Nano* **2011**, *5*, 1459.
[49] H. Li, G. Gordeev, S. Wasserroth, V. S. K. Chakravadhanula, S. K. C. Neelakandhan, F. Hennrich, A. Jorio, S. Reich, R. Krupke, B. S. Flavel, *Nat. Nanotechnol.* **2017**, *12*, 1176.
[50] A. G. Souza Filho, M. Endo, H. Muramatsu, T. Hayashi, Y. A. Kim, E. B. Barros, N. Akuzawa, G. G. Samsonidze, R. Saito, M. S. Dresselhaus, *Phys. Rev. B* **2006**, *73*, 235413.
[51] J. Wei, B. Jiang, X. Zhang, H. Zhu, D. Wu, *Chem. Phys. Lett.* **2003**, *376*, 753.
[52] A. Jorio, C. Fantini, M. A. Pimenta, R. B. Capaz, G. G. Samsonidze, G. Dresselhaus, M. S. Dresselhaus, J. Jiang, N. Kobayashi, A. Grüneis, R. Saito, *Phys. Rev. B* **2005**, *71*, 075401.
[53] H. Kataura, Y. Kumazawa, Y. Maniwa, I. Umezu, S. Suzuki, Y. Ohtsuka, Y. Achiba, *Synth. Met.* **1999**, *103*, 2555.
[54] G. G. Samsonidze, R. Saito, N. Kobayashi, A. Grüneis, J. Jiang, A. Jorio, S. G. Chou, G. Dresselhaus, M. S. Dresselhaus, *Appl. Phys. Lett.* **2004**, *85*, 5703.
[55] E. B. Barros, H. Son, G. G. Samsonidze, A. G. Souza Filho, R. Saito, Y. A. Kim, H. Muramatsu, T. Hayashi, M. Endo, J. Kong, M. S. Dresselhaus, *Phys. Rev. B* **2007**, *76*, 045425.
[56] A. Botello-Méndez, J. Campos-Delgado, A. Morelos-Gómez, J. M. Romo-Herrera, Á. G. Rodríguez, H. Navarro, M. A. Vidal, H. Terrones, M. Terrones, *Chem. Phys. Lett.* **2008**, *453*, 55.
[57] J.-Y. Mevellec, C. Bergeret, J. Cousseau, J.-P. Buisson, C. P. Ewels, S. Lefrant, *J. Am. Chem. Soc.* **2011**, *133*, 16938.
[58] Y. J. Lee, S. R. Ham, J. H. Kim, T. H. Yoo, S. R. Kim, Y. T. Lee, D. K. Hwang, B. Angadi, W. S. Seo, B. K. Ju, W. K. Choi, *Sci. Rep.* **2018**, *8*, 4851.
[59] L. Shi, J. Wei, K. Yanagi, T. Saito, K. Cao, U. Kaiser, P. Ayala, T. Pichler, *Nanoscale* **2018**, *10*, 21254.
[60] K. E. Moore, B. S. Flavel, A. V. Ellis, J. G. Shapter, *Carbon N. Y.* **2011**, *49*, 2639.
[61] H. Park, P. R. Brown, V. Bulović, J. Kong, *Nano Lett.* **2012**, *12*, 133.
[62] H. Kinoshita, I. Jeon, M. Maruyama, K. Kawahara, Y. Terao, D. Ding, R. Matsumoto, Y. Matsuo, S. Okada, H. Ago, Adv. Mater. **2017**, *29*, 1702141.
[63] K. Cui, Y. Qian, I. Jeon, A. Anisimov, Y. Matsuo, E. I. Kauppinen, S. Maruyama, *Adv. Energy Mater.* **2017**, *7*, 1700449.
[64] I. Jeon, C. Delacou, A. Kaskela, E. I. Kauppinen, S. Maruyama, Y. Matsuo, *Sci. Rep.* **2016**, *6*, 31348.
[65] H. Do Kim, Y. Miyamoto, H. Kubota, T. Yamanari, H. Ohkita, *Chem. Lett.* **2017**, *46*, 253.
[66] Q. Wang, Y. Shao, Q. Dong, Z. Xiao, Y. Yuan, J. Huang, *Energy Environ. Sci.* **2014**, *7*, 2359.
[67] I. Jeon, Y. Matsuo, *Sol. Energy Mater. Sol. Cells* **2015**, *140*, 335.
[68] F. Xia, Q. Wu, P. Zhou, Y. Li, X. Chen, Q. Liu, J. Zhu, S. Dai, Y. Lu, S. Yang, *ACS Appl. Mater. Interfaces* **2015**, *7*, 13659.
[69] I. Jeon, J. W. Ryan, T. Nakazaki, K. S. Yeo, Y. Negishi, Y. Matsuo, *J. Mater. Chem. A* **2014**, *2*, 18754.
[70] H. Qian, P. T. Araujo, C. Georgi, T. Gokus, N. Hartmann, A. A. Green, A. Jorio, M. C. Hersam, L. Novotny, A. Hartschuh, *Nano Lett.* **2008**, *8*, 2706.
[71] H. Dong, Z. Wu, J. Xi, X. Xu, L. Zuo, T. Lei, X. Zhao, L. Zhang, X. Hou, A. K.-Y. Jen,

Adv. Funct. Mater. **2018**, *28*, 1704836.
[72] J. Lee, H. Kang, G. Kim, H. Back, J. Kim, S. Hong, B. Park, E. Lee, K. Lee, *Adv. Mater.* **2017**, *29*, 1606363.
[73] J.-W. Lee, S.-H. Bae, Y.-T. Hsieh, N. De Marco, M. Wang, P. Sun, Y. Yang, *Chem* **2017**, *3*, 290.
[74] N. Ahn, K. Kwak, M. S. Jang, H. Yoon, B. Y. Lee, J. Lee, P. V Pikhitsa, J. Byun, M. Choi, *Nat. Commun.* **2016**, *7*, 13422.
[75] J. P. Perdew, K. Burke, M. Ernzerhof, *Phys. Rev. Lett.* **1996**, *77*, 3865.
[76] S. Peng, K. Cho, *Nano Lett.* **2003**, *3*, 513.
[77] W. Tang, E. Sanville, G. Henkelman, *J. Phys. Condens. Matter* **2009**, *21*, 084204.
[78] J. Han, S. Yuan, L. Liu, X. Qiu, H. Gong, X. Yang, C. Li, Y. Hao, B. Cao, *J. Mater. Chem. A* **2015**, *3*, 5375.
[79] Y. Jin, Y. Sun, K. Wang, Y. Chen, Z. Liang, Y. Xu, F. Xiao, *Nano Res.* **2018**, *11*, 1998.
[80] E. Lee, J. Ahn, H.-C. Kwon, S. Ma, K. Kim, S. Yun, J. Moon, *Adv. Energy Mater.* **2018**, *8*, 1702182.
[81] H. Chen, M. Li, X. Wen, Y. Yang, D. He, W. Choy, H. Lu, *Nanomaterials* **2019**, *9*, 193.
[82] S. Kang, J. Jeong, S. Cho, Y. J. Yoon, S. Park, S. Lim, J. Y. Kim, H. Ko, *J. Mater. Chem. A* **2019**, *7*, 1107.
[83] Q. Luo, H. Ma, Q. Hou, Y. Li, J. Ren, X. Dai, Z. Yao, Y. Zhou, L. Xiang, H. Du, H. He, N. Wang, K. Jiang, H. Lin, H. Zhang, Z. Guo, *Adv. Funct. Mater.* **2018**, 1706777.
[84] S. Liu, K. Cao, H. Li, J. Song, J. Han, Y. Shen, M. Wang, *Solar Energy* **2017**, *144*, 158.
[85] Q. Luo, H. Ma, F. Hao, Q. Hou, J. Ren, L. Wu, Z. Yao, Y. Zhou, N. Wang, K. Jiang, H. Lin, Z. Guo, *Adv. Funct. Mater.* **2017**, 1703068.
[86] X. Zheng, H. Chen, Q. Li, Y. Yang, Z. Wei, Y. Bai, Y. Qiu, D. Zhou, K. S. Wong, S. Yang, *Nano Lett.* **2017**, *17*, 2496.
[87] Q. Luo, H. Ma, Y. Zhang, X. Yin, Z. Yao, N. Wang, J. Li, S. Fan, K. Jiang, H. Lin, *J. Mater. Chem. A*, **2016**, *4*, 5569.
[88] H. Li, K. Cao, J. Cui, S. Liu, X. Qiao, Y. Shen, M. Wang, *Nanoscale* **2016**, *8*, 6379.
[89] Z. Wei, H. Chen, K. Yan, X. Zheng, S. Yang, *J. Mater. Chem. A* **2015**, *3*, 24226.
[90] R. Li, X. Xiang, X. Tong, J. Zou, Q. Li, *Adv. Mater.* **2015**, *27*, 3831.
[91] X. Wang, Z. Lia,W. Xu, S. A.Kulkarni, S. K. Batabyal, S. Zhang, A. Cao, L. H. Wong, *Nano Energy* **2015,** *11*, 728.
[92] Z. Li, S. A. Kulkarni, P. P. Boix, E. Shi, A. Cao, K. Fu, S. K. Batabyal, J. Zhang, Q. Xiong, L. H. Wong, N. Mathews, S. G. Mhaisalkar, *ACS Nano* **2014**, *8*, 6797.

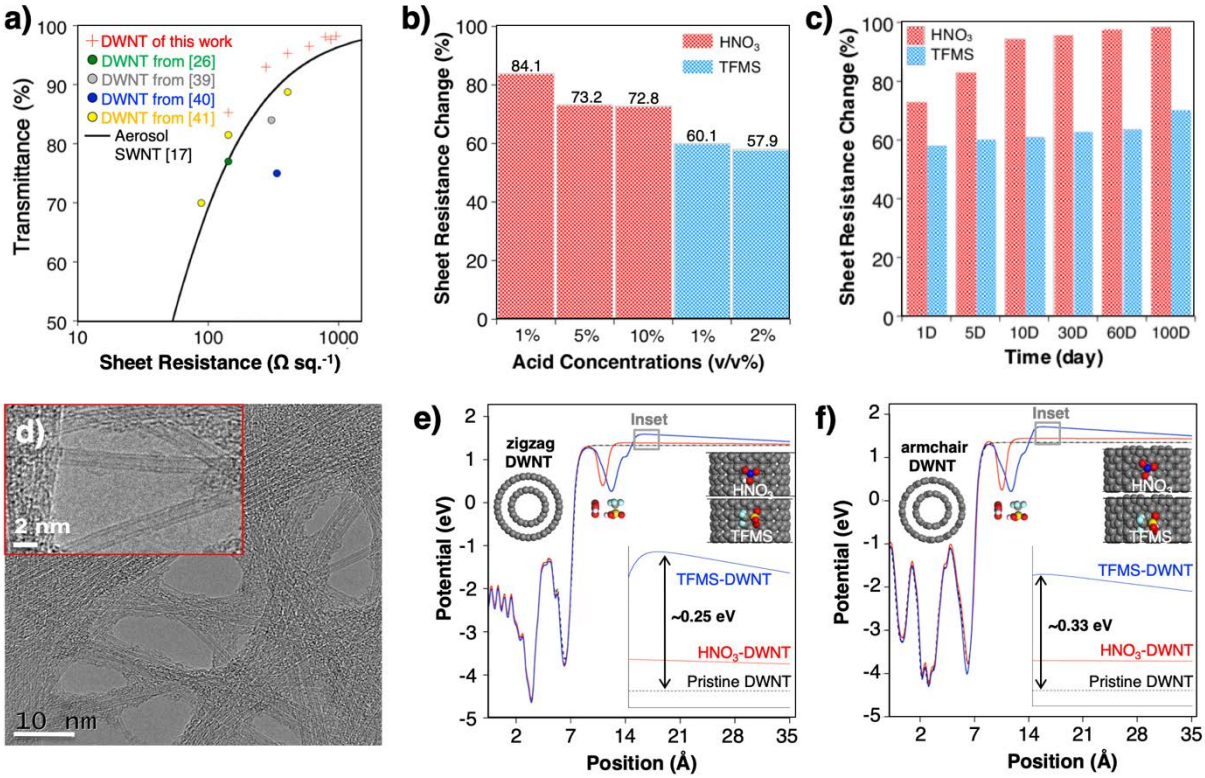

Figure 1. a) Transmittance over sheet resistance data plots of DWNT films in this work compared with previously reported DWNT films and aerosol-synthesized SWNT films.[26,39–41] b) Bar graph showing the sheet resistance change of DWNT films upon HNO_3 doping (red) and TFMS doping (blue) in different concentration. c) Bar graph showing the doping durability of HNO_3-doped DWNT films (red) and TFMS-doped DWNT films (blue). d) TEM image of a DWNT film and a magnified image as an inset. DFT-calculated potential energy change of e) zigzag DWNTs (simulating a semiconducting DWNT) and f) armchair DWNTs (simulating a metallic DWNT) upon HNO_3 (red) and TFMS (blue) doping.

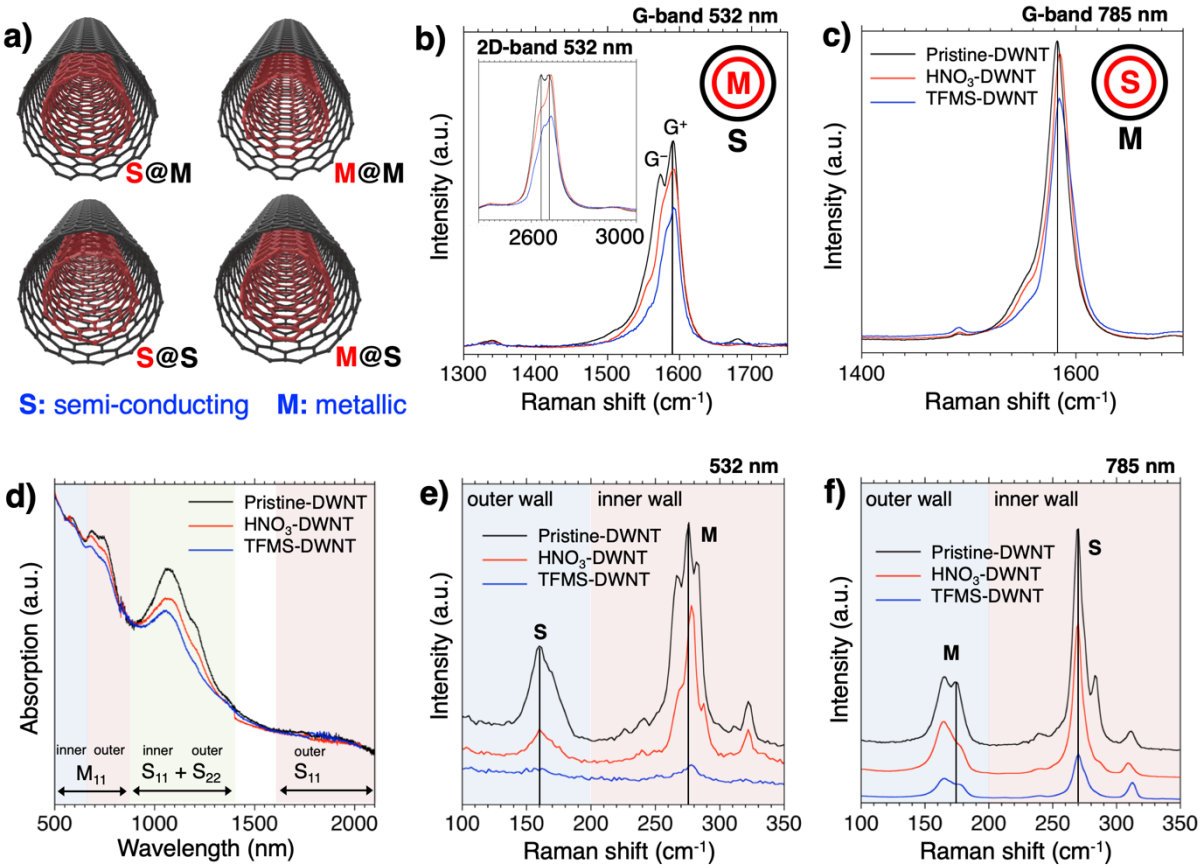

Figure 2. a) 3D rendered illustration of four different permutations of DWNT, where outer walls are shown in black and inner walls are shown in red. S indicates semi-conducting nanotubes and M indicates metallic nanotubes. b–c) Raman spectra of G-bands of pristine DWNT films (black line), HNO_3-doped DWNT films (red line), and TFMS-doped DWNT films (blue line) b) under a 532 nm laser line, where 2D-band is also shown as an inset, and c) under a 785 nm laser line. d) Vis-NIR spectra of pristine DWNT films (black line), HNO_3-doped DWNT films (red line), and TFMS-doped DWNT films (blue line). e–f) Raman spectra at the RMB region of pristine DWNT films (black line), HNO_3-doped DWNT films (red line), and TFMS-doped DWNT films (blue line) under e) a 532 nm laser line and f) a 785 nm laser line.

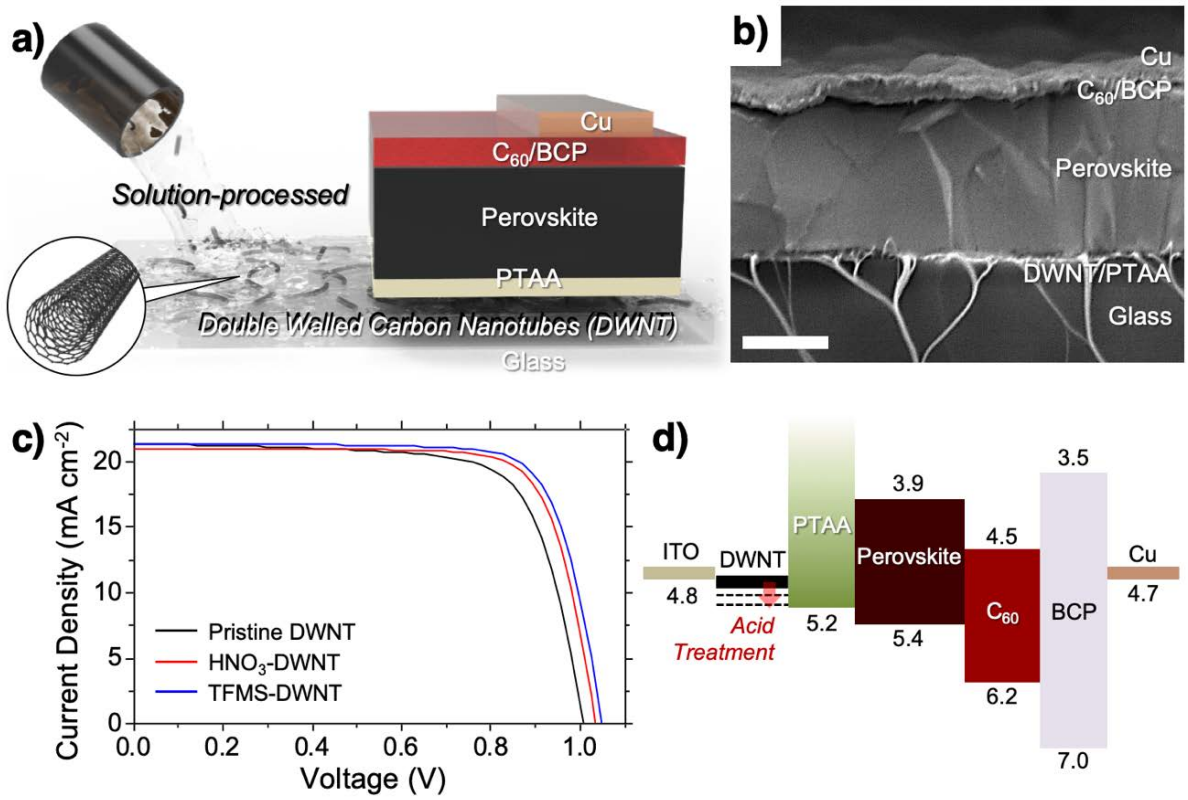

Figure 3. a) Schematic illustration of a PSC structure employing solution-processed DWNTs as the transparent electrode. b) Cross-sectional SEM image of a PSC employing the DWNT electrode (scale bar: 300 nm). c) *J*–*V* curves of the best-performing DWNT-PSCs with and without the acid treatments. d) Energy level diagram of the PSCs fabricated in this work.

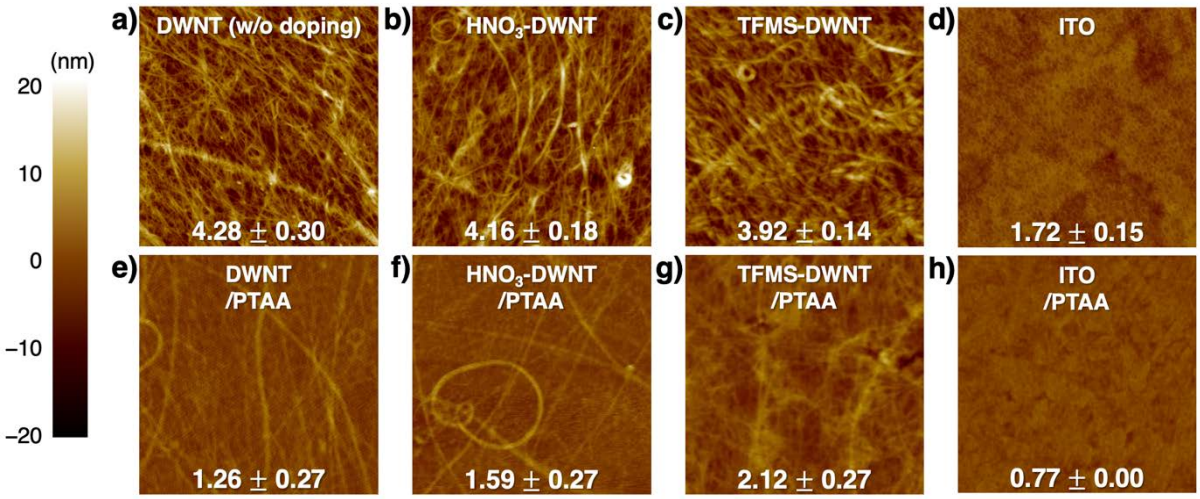

Figure 4. AFM surface topography images (2.5 × 2.5 μm^2) of a) a pristine DWNT film, b) a HNO_3-doped DWNT film, c) a TFMS-doped DWNT film, d) ITO, and e–h) PTAA-coated DWNT films and ITO. RMS roughness values with standard deviations are displayed on each image.

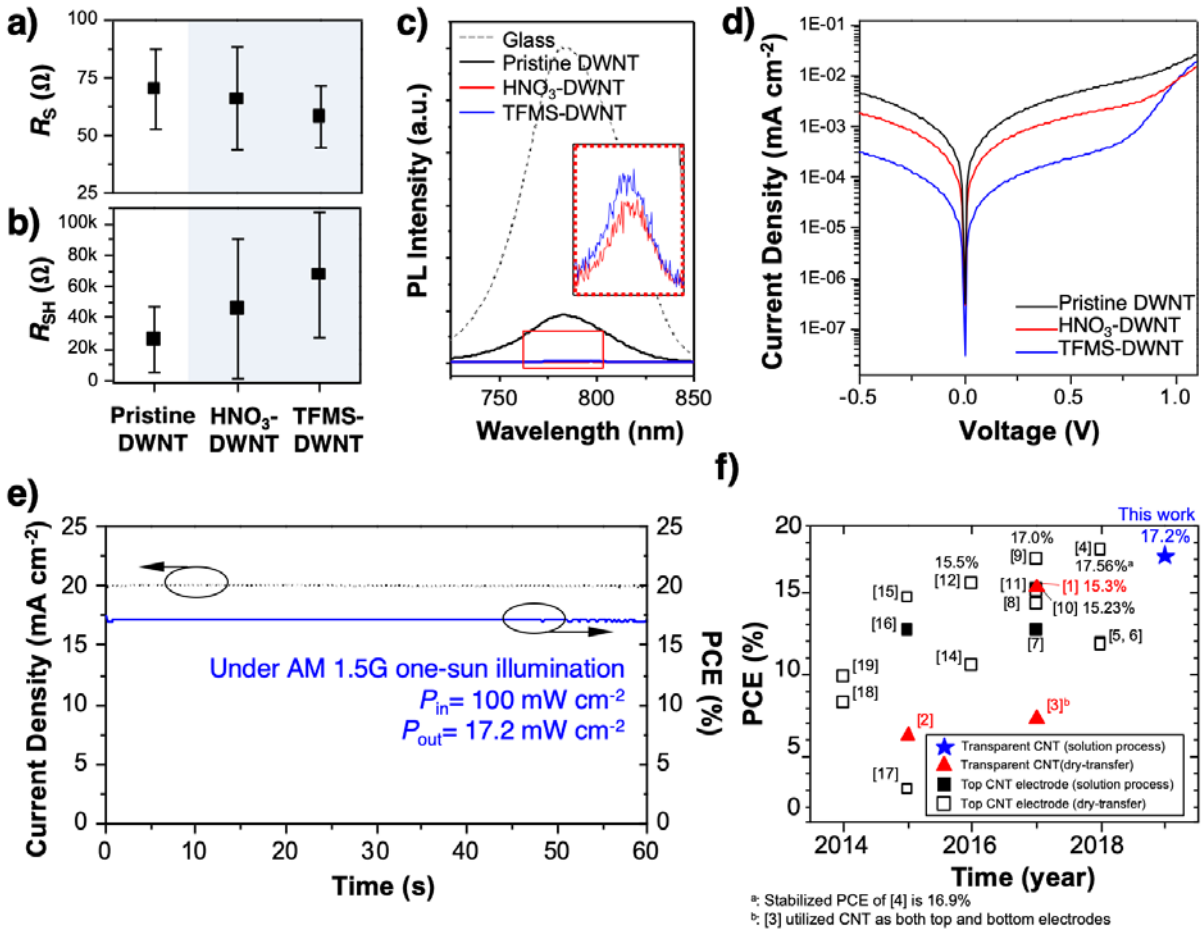

Figure 5. a) Series resistance and b) shunt resistance of the DWNT-based PSCs obtained from *J*–*V* curves measured under AM 1.5G one-sun illumination. c) Steady-state PL spectra of the perovskite film on glass (dotted line), PTAA-coated DWNT (black solid line), PTAA-coated HNO_3-doped DWNT (red solid line), and PTAA-coated TFMS-doped DWNT (blue solid line). d) *J*–*V* curves of the DWNT-based PSCs under dark condition. e) Stabilized current density and PCE of a TFMS-doped DWNT-based PSC measured under the maximum power point condition (applied voltage: 0.86 V) and AM 1.5G one-sun illumination (100 mW cm^{-2}). f) Plot containing the photovoltaic performance and electrode information of the reported PSCs in which CNT was used for bottom and top electrodes.[6,7,12–16, 42, 83–92]

Table 1. Charge transfer between DWNT and dopants calculated using the Bader charge analysis (derived from Table S3).

Charge transfer per molecule[a]	Zigzag DWNT		Armchair DWNT	
	HNO_3	TFMS	HNO_3	TFMS
Inner wall of DWNT	+0.0001 e^-	–0.0028 e^-	–0.0056 e^-	–0.0042 e^-
Outer wall of DWNT	–0.0169 e^-	–0.0326 e^-	–0.0154 e^-	–0.0459 e^-
Dopant	+0.0168 e^-	+0.0354 e^-	+0.0210 e^-	+0.0500 e^-

a: The calculated charge transfer value is small, because it was calculated in a closed system. An actual environment will be an open system, in which the charge transfer value will be much greater.

Table 2. Average and best photovoltaic parameter values of the DWNT-based PSCs under AM 1.5G one-sun illumination.

Anode		V_{OC} (V)	J_{SC} (mA cm^{-2})	FF	PCE (%)
Pristine DWNT	Average	0.99 ±0.01	20.9 ±0.6	69.1 ±3.9	14.4 ±1.1
	Best	1.01	21.4	72.5	15.6
HNO_3-doped DWNT	Average	1.01 ±0.03	20.0 ±1.1	71.7 ±6.2	15.6 ±2.1
	Best	1.04	20.7	74.2	16.7
TFMS-doped DWNT	Average	1.02 ±0.02	21.0 ±1.0	75.0 ±2.4	16.0 ±1.1
	Best	1.05	21.4	77.1	17.2

Solution-processed double-walled carbon nanotubes function as transparent electrodes in inverted-type planar heterojunction perovskite solar cells. Double-walled carbon nanotubes exhibit high optical conductivity and solubility. Good energy level alignment and morphology of the electrodes lead to an operating power conversion efficiency of 17.2%, which is the highest among the carbon nanotube electrode-based perovskite solar cells.

Keywords: Double-walled nanotubes, Solution-processed electrode, Transparent electrode, Indium-free, Perovskite solar cells

I. Jeon, J. Yoon, U. Kim, C. Lee, R. Xiang, A. Shawky, J. Xi, J. Byeon, H. M. Lee, M. Choi*, S. Maruyama*, Y. Matsuo*

High-Performance Solution-Processed Double-walled Carbon Nanotube Transparent Electrode for Perovskite Solar Cells

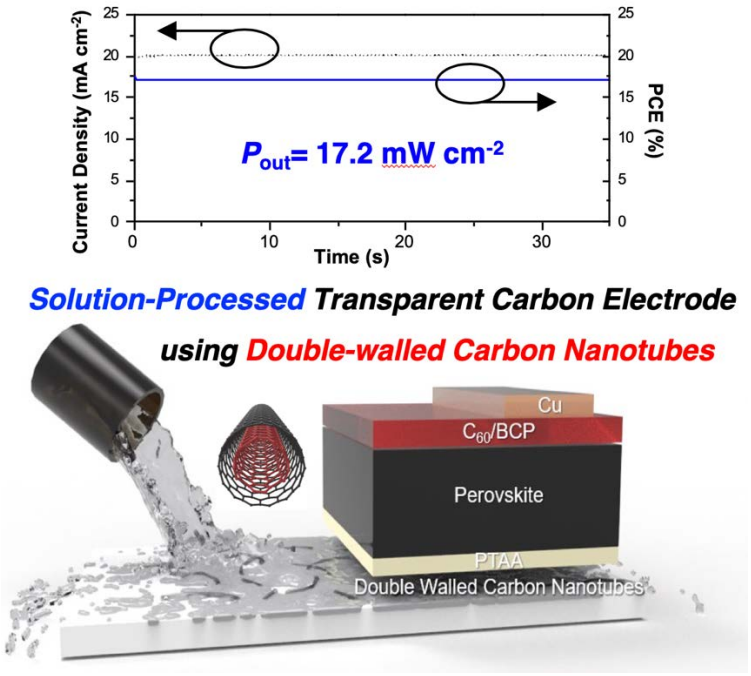

Supporting Information

High-Performance Solution-Processed Double-walled Carbon Nanotube Transparent Electrode for Perovskite Solar Cells

Il Jeon, Jungjin Yoon, Unsoo Kim, Changsoo Lee, Rong Xiang, Ahmed Shawky, Jun Xi, Junseop Byeon, Hyuck Mo Lee, Mansoo Choi, Shigeo Maruyama*, and Yutaka Matsuo**

Figure S1. A picture of slot-die coated DWNT electrode on a large glass substrate.

Table S1. Sheet resistance of pristine DWNT films and HNO_3- and TFMS-doped DWNT films measured by the van der Pauw method.

	HNO_3 (Ω sq.$^{-1}$)			TFMS (Ω sq.$^{-1}$)	
	1 v/v%	**5 v/v%**	**10 v/v%**	**1 v/v%**	**2 v/v%**
Pristine	148 ±14	133 ±11	142 ±10	153 ±13	129 ±12
After Doping	125 ±28	97 ±26	103 ±24	92 ±27	74 ±24

Table S2. Sheet resistance change of the HNO_3- and TFMS-doped DWNT films over days left in ambience.

	HNO_3 (Ω sq.$^{-1}$)	TFMS (Ω sq.$^{-1}$)
	10 v/v%	**2 v/v%**
Pristine	142 ±10	129 ±12
After 1D	103 ±14	74 ±24
After 5D	118 ±31	77 ±20
After 10D	134 ±14	79 ±28
After 30D	136 ±15	81 ±21
After 60D	138 ±17	82 ±11
After 100D	140 ±13	90 ±27

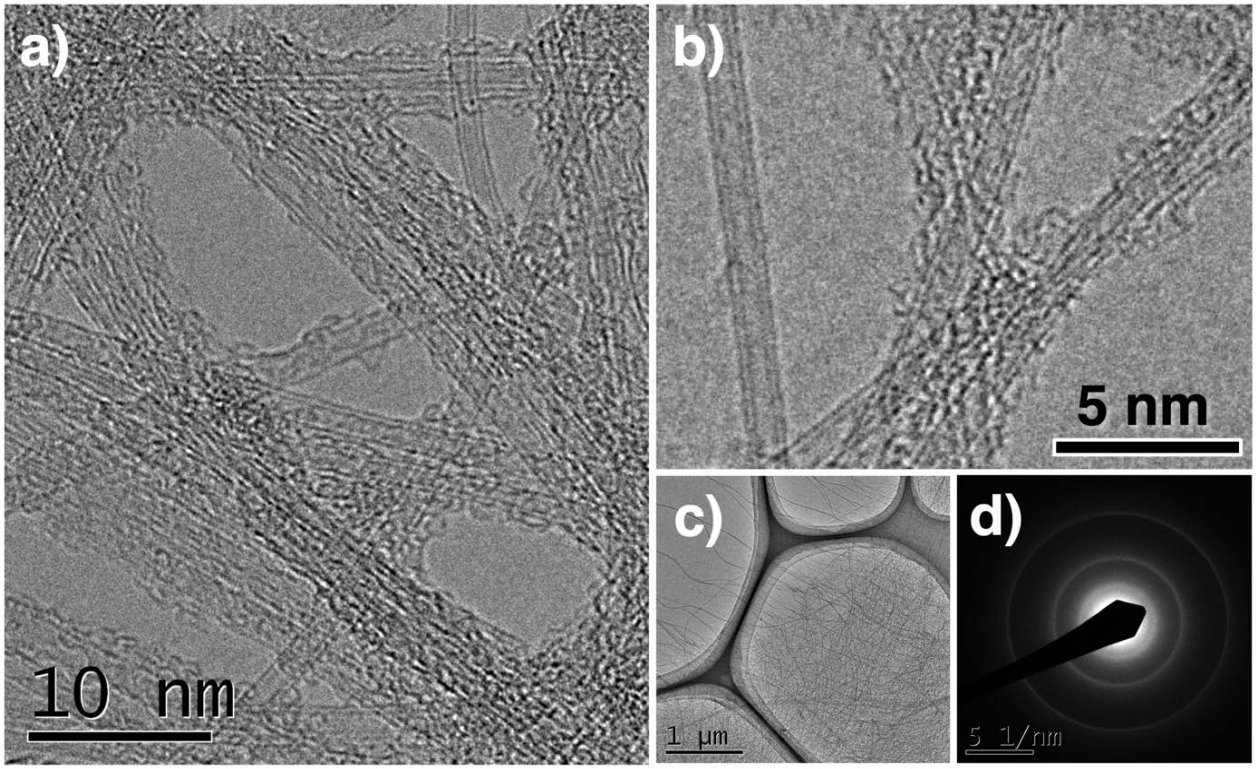

Figure S2. TEM images of DWNTs with a scale bar of a) 10 nm, b) 5 nm, and c) 1 µm. d) SAED of the same DWNT sample.

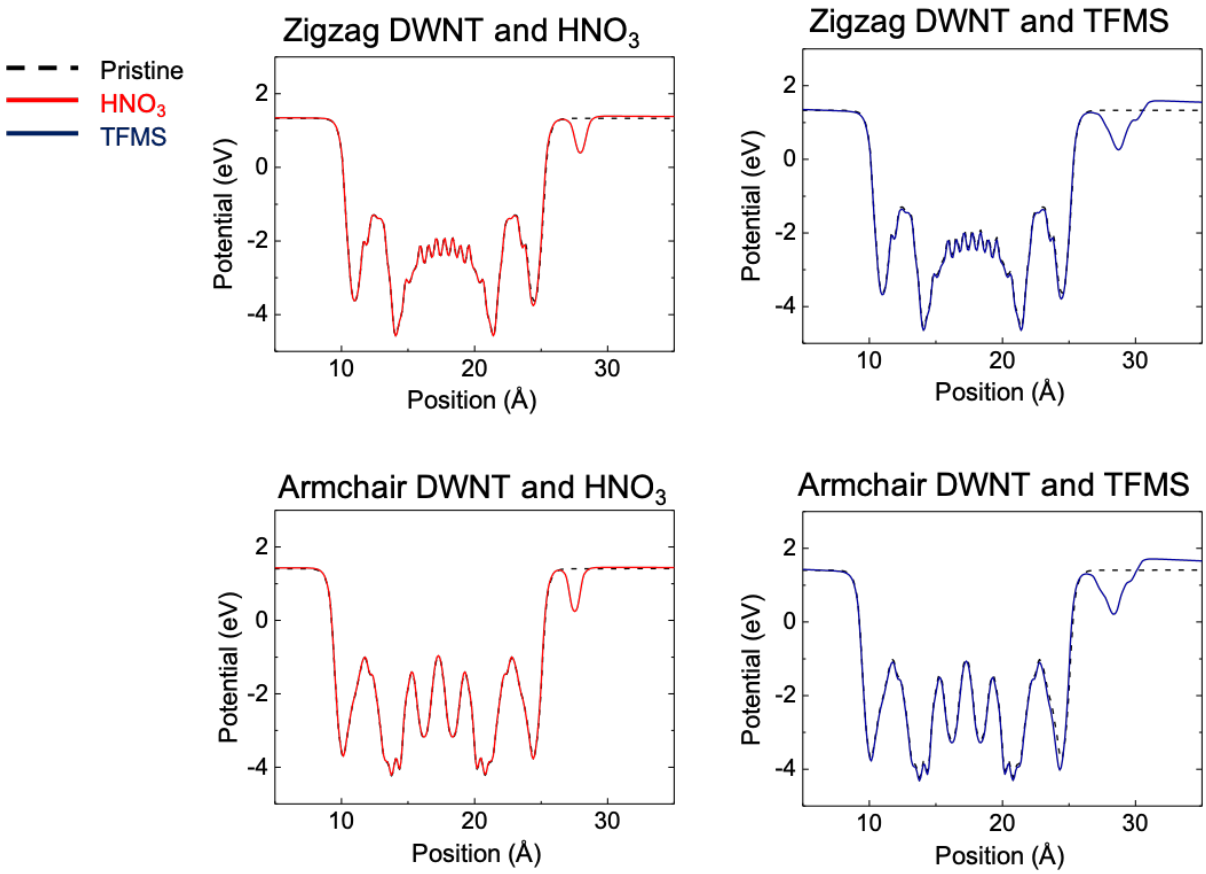

Figure S3. DFT-calculated potential energy change of zigzag DWNTs armchair DWNTs upon HNO_3 and TFMS doping.

Table S3. Charge transfer of inner walls and outer walls within DWNTs before and after HNO_3 and TFMS doping calculated using the Bader charge analysis.

Charge transfer per molecule[a]		Zigzag DWNT		Armchair DWNT	
		HNO_3	TFMS	HNO_3	TFMS
Pristine	Inner wall of DWNT	+0.1520 e^-		+0.0240 e^-	
	Outer wall of DWNT	–0.1520 e^-		–0.0240 e^-	
Next to dopants	Inner wall of DWNT	+0.1521 e^-	+0.1492 e^-	+0.0184 e^-	+0.0192 e^-
	Outer wall of DWNT	–0.1689 e^-	–0.1846 e^-	–0.0394 e^-	–0.0699 e^-
	Acid Dopants	+0.0168 e^-	+0.0354 e^-	+0.0210 e^-	+0.0500 e^-

a: The calculated charge transfer value is small, because it was calculated in a closed system. An actual environment will be an open system, in which the charge transfer value will be much greater.

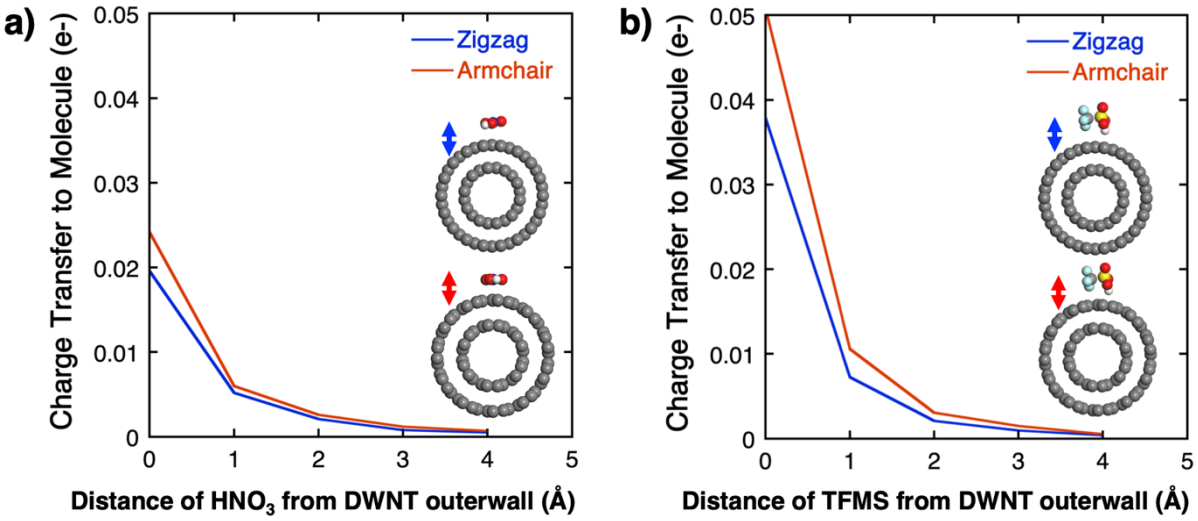

Figure S4. DFT-calculated binding energy between a DWNT and a dopant as the distance increases for a) HNO_3 and b) TFMS.

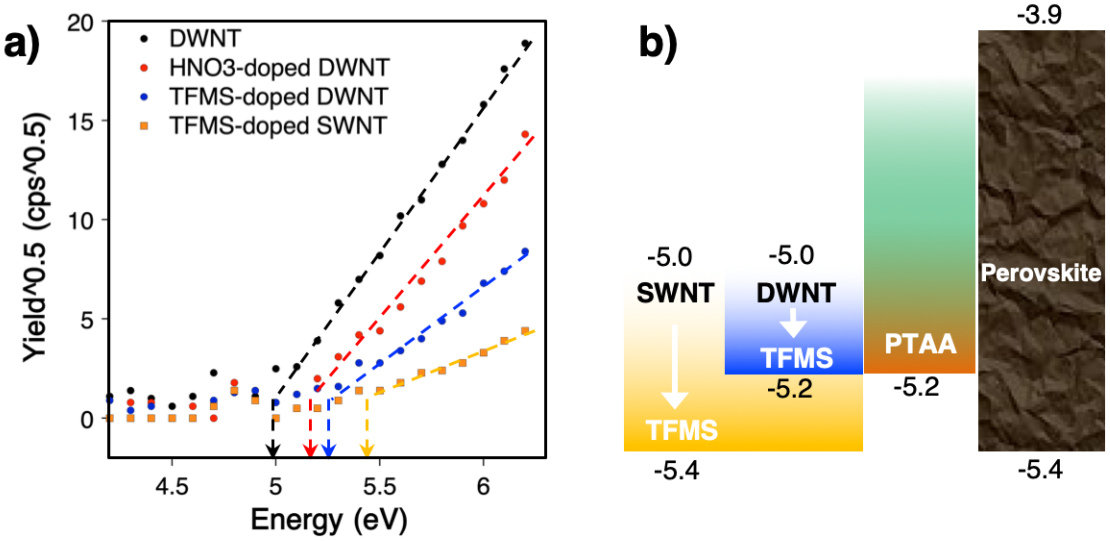

Figure S5. a) PYS measurement of a pristine DWNT film, a HNO_3-doped DWNT film, a TFMS-doped DWNT film, and a TFMS-doped SWNT film. b) Energy level diagram based on the measurement of PYS.

Table S4. Previously reported V_{OC} of SWNT transparent electrode-based PSCs.

Electrode	Charge selection layer	Solar cell type	Reported V_{OC} (V)	Reference no.
HNO_3-doped SWNT	PEDOT:PSS[a]	Perovskite	0.79	[6]
ITO			0.83	
MoO_x-doped SWNT	PEDOT:PSS	Perovskite	0.90	[7]
MoO_x-doped graphene			0.97	
ITO			0.96	
MoO_x-doped SWNT	PEDOT:PSS	Organic	0.72	[10]
ITO			0.74	
Polymer-doped SWNT	MoO_3	Organic	0.80	[11]
ITO			0.81	
HNO_3-doped SWNT	PEDOT:PSS	Perovskite	0.81	[42]
ITO			0.93	

a: PEDOT:PSS = poly(3,4-ethylenedioxythiophene)

Table S5. Average and best photovoltaic parameter values of the ITO-based PSCs under AM 1.5G one-sun illumination.

Anode		V_{OC} (V)	J_{SC} (mA cm^{-2})	FF	PCE (%)
ITO	Average	1.05 ±0.01	22.9 ±0.2	75.3 ±1.9	18.1 ±0.6
	Best	1.06	22.9	77.9	19.0

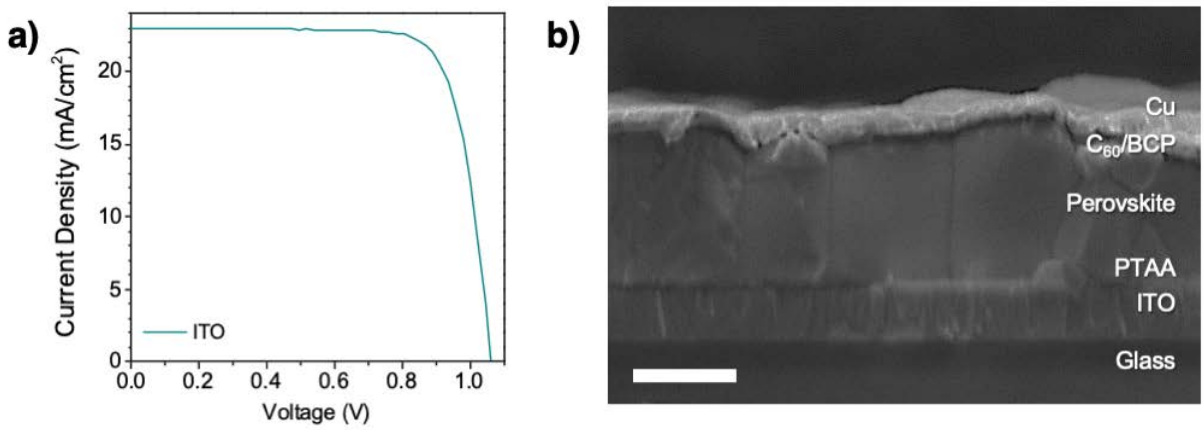

Figure S6. a) *J–V* curve of the ITO-based PSC and b) its cross-sectional SEM image (scale bar: 300 nm).

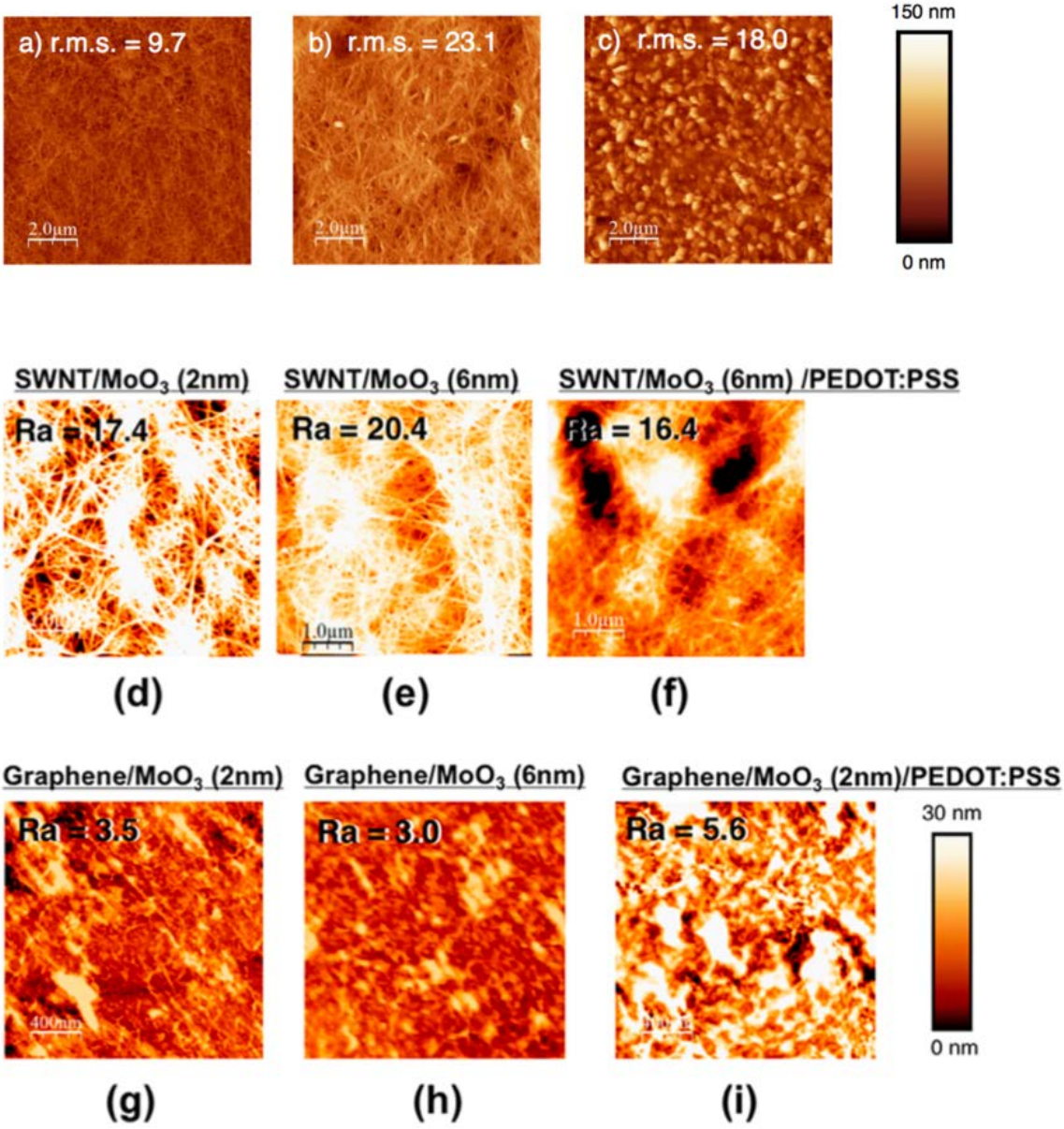

Figure S7. AFM images with RMS roughness values of a) a SWNT film, b) a SWNT film with MoO_x on top, and c) a SWNT film with MoO_x and PEDOT:PSS. Reproduced with permission.[10] Copyright 2015, American Chemical Society. AFM images with average roughness (*R*a) values of d) a SWNT film, e) a 6nm-thick MoO_3-deposited SWNT film, f) a 6nm-thick MoO_3-deposited SWNT film with a PEDOT:PSS overcoat, g) a graphene film, h) a graphene film with 2 nm-thick MoO_3, and i) a 2 nm-thick MoO_3-deposited graphene with a PEDOT:PSS overcoat. Reproduced with permission.[7] Copyright 2017, American Chemical Society.

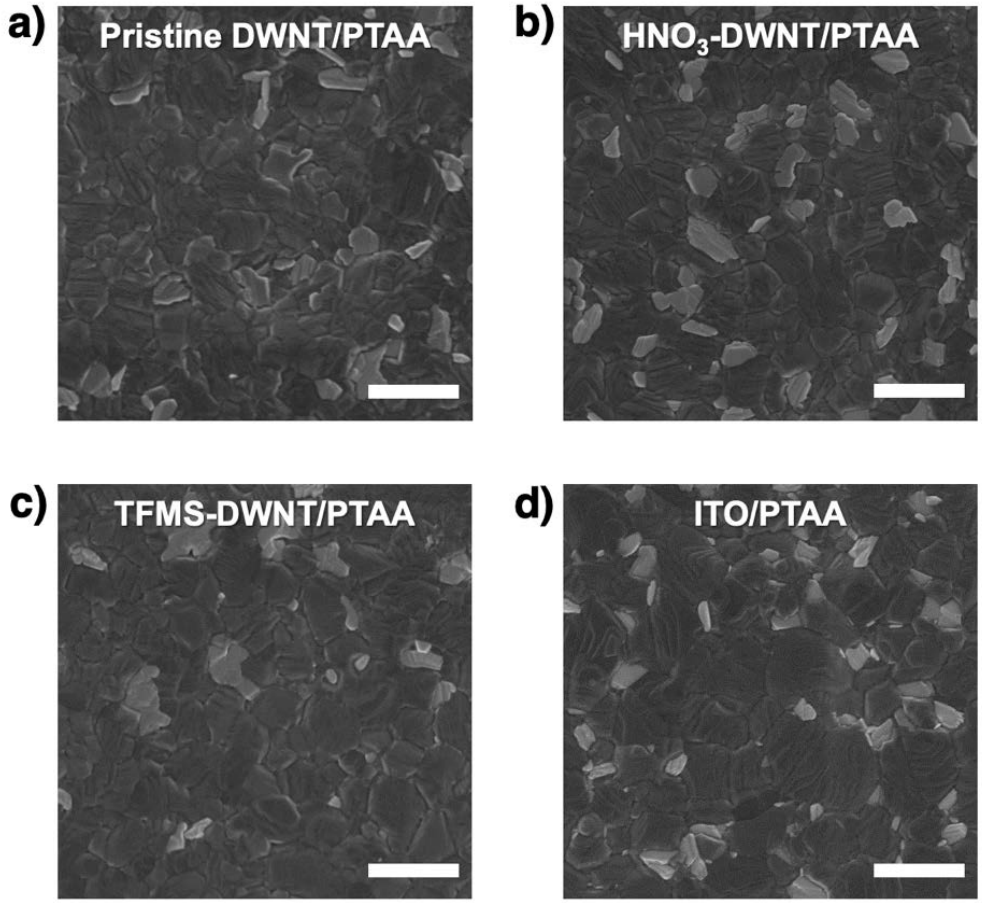

Figure S8. Plane-view SEM images of perovskite layer fabricated on a) pristine DWNT/ PTAA, b) HNO_3-doped DWNT/PTAA, c) TFMS-doped DWNT/PTAA, d) ITO/PTAA (Scale bar: 1 μm).

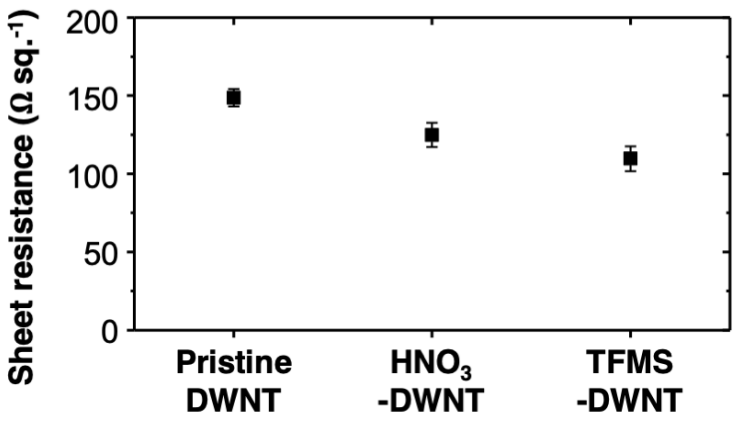

Figure S9. Sheet resistance of the DWNT electrodes used for the PSC fabrication.

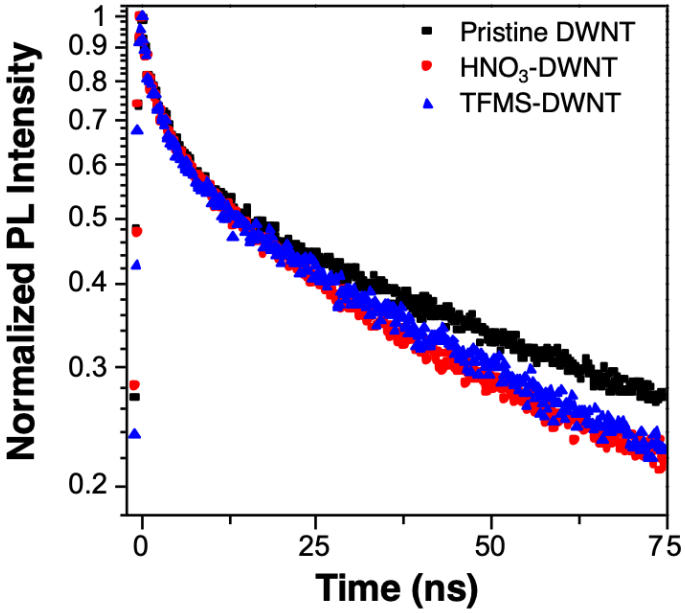

Figure S10. Normalized (TRPL) spectra of perovskite layers on a PTAA-coated pristine DWNT film (black), a PTAA-coated HNO_3-doped DWNT film (red), and a PTAA-coated TFMS-doped DWNT film (blue).

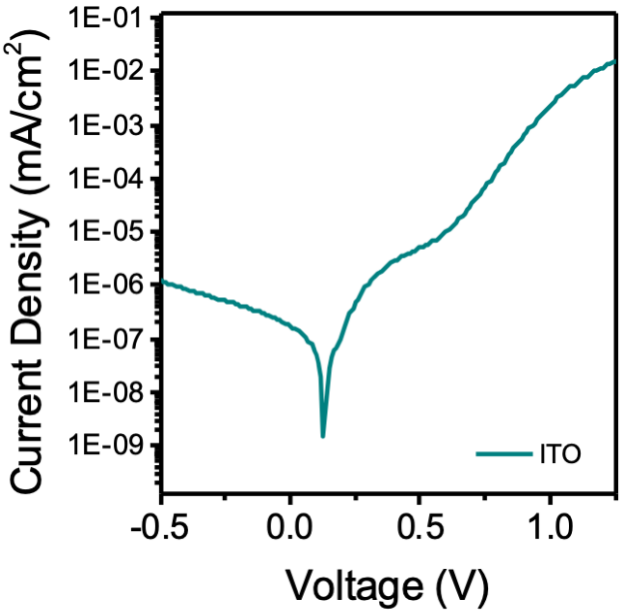

Figure S11. Dark *J*–*V* curve of the ITO-based PSCs.

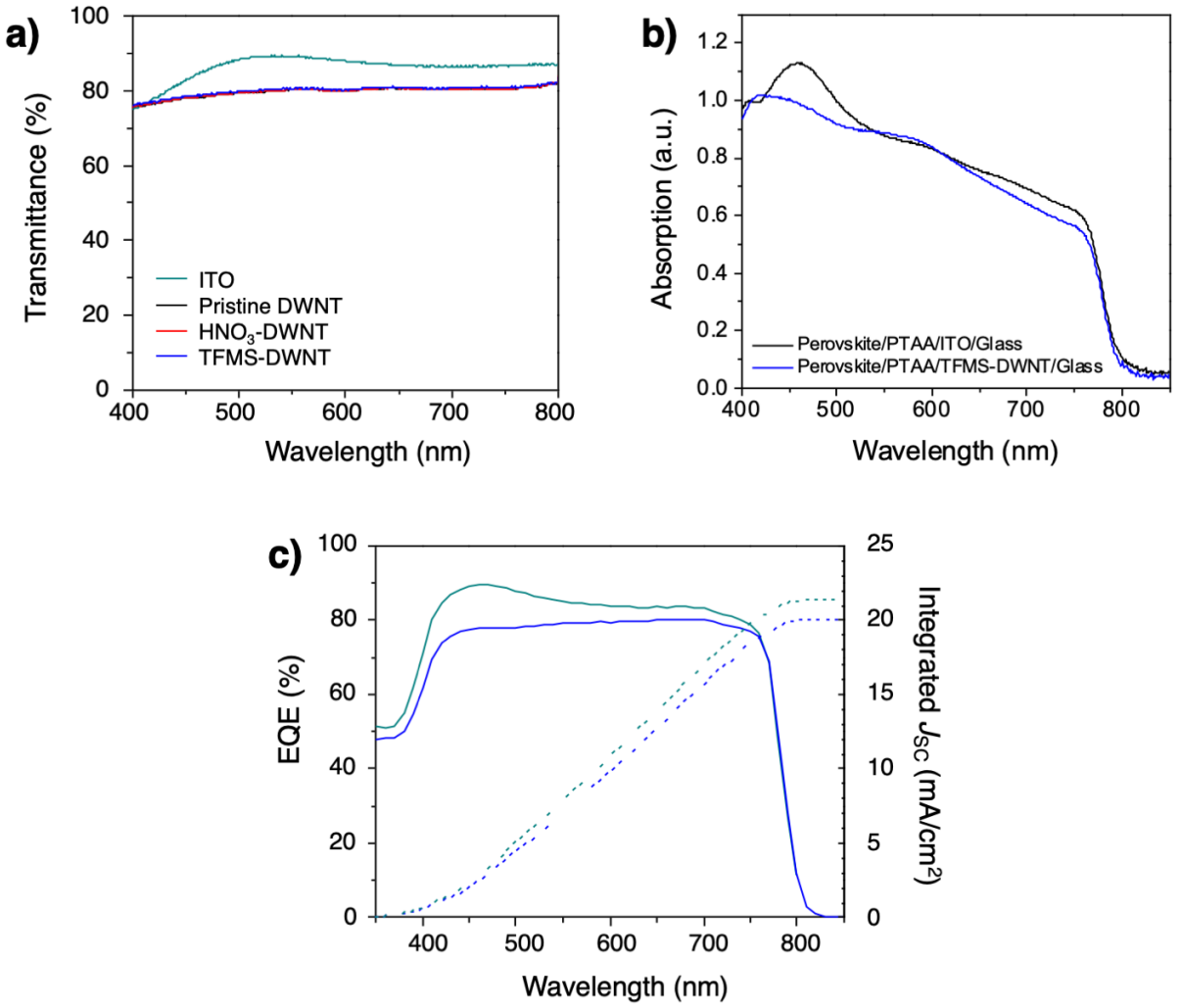

Figure S12. a) Optical transmittance spectra of ITO (jade), a pristine DWNT film (black), a HNO_3-doped DWNT film (red), and a TFMS-doped DWNT film (blue) on glass substrates. b) Absorption spectra of perovskite films fabricated on PTAA/ITO/Glass (black) and on PTAA/TFMS-doped DWNT/Glass (blue). c) External quantum efficiency spectra (solid line) and integrated J_{SC} curves (dotted line) of the DWNT (blue)- and ITO (cyan)- based PSCs.

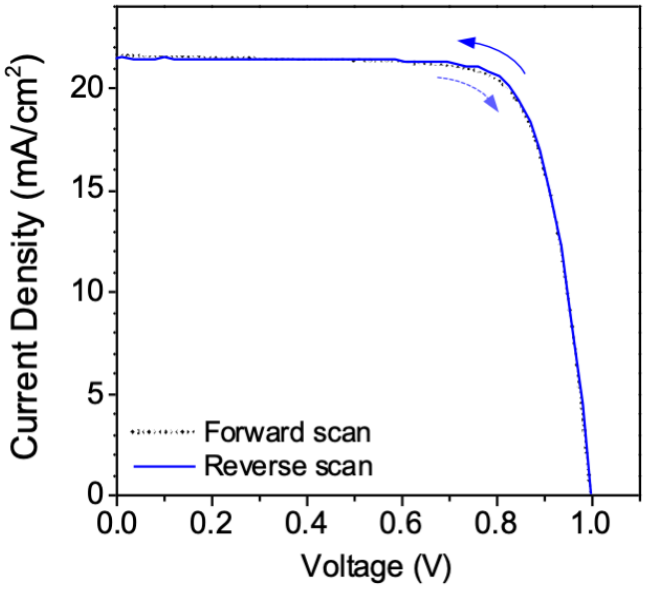

Figure S13. *J*–*V* curves of a TFMS-doped DWNT-based PSC with different voltage sweep directions.

Table S6. Photovoltaic performance parameters of a TFMS-doped DWNT-based device depicted in Figure S13.

Sweep direction	V_{OC} (V)	J_{SC} (mA cm^{-2})	FF (%)	PCE (%)
Reverse	1.00	21.5	77.5	16.6
Forward	1.00	21.6	76.0	16.4

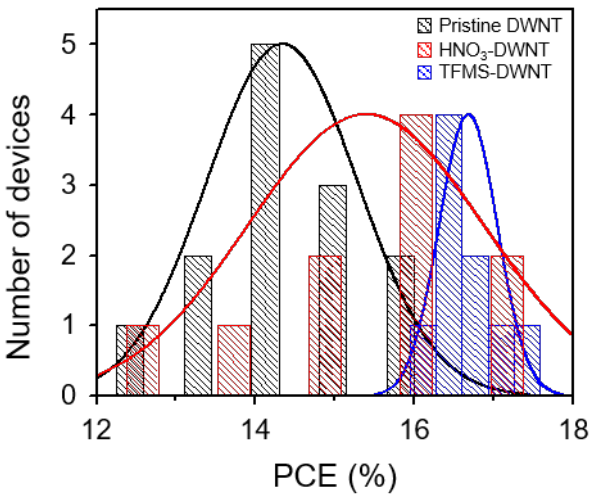

Figure S14. Statistical analysis histogram of DWNT-based PSCs.

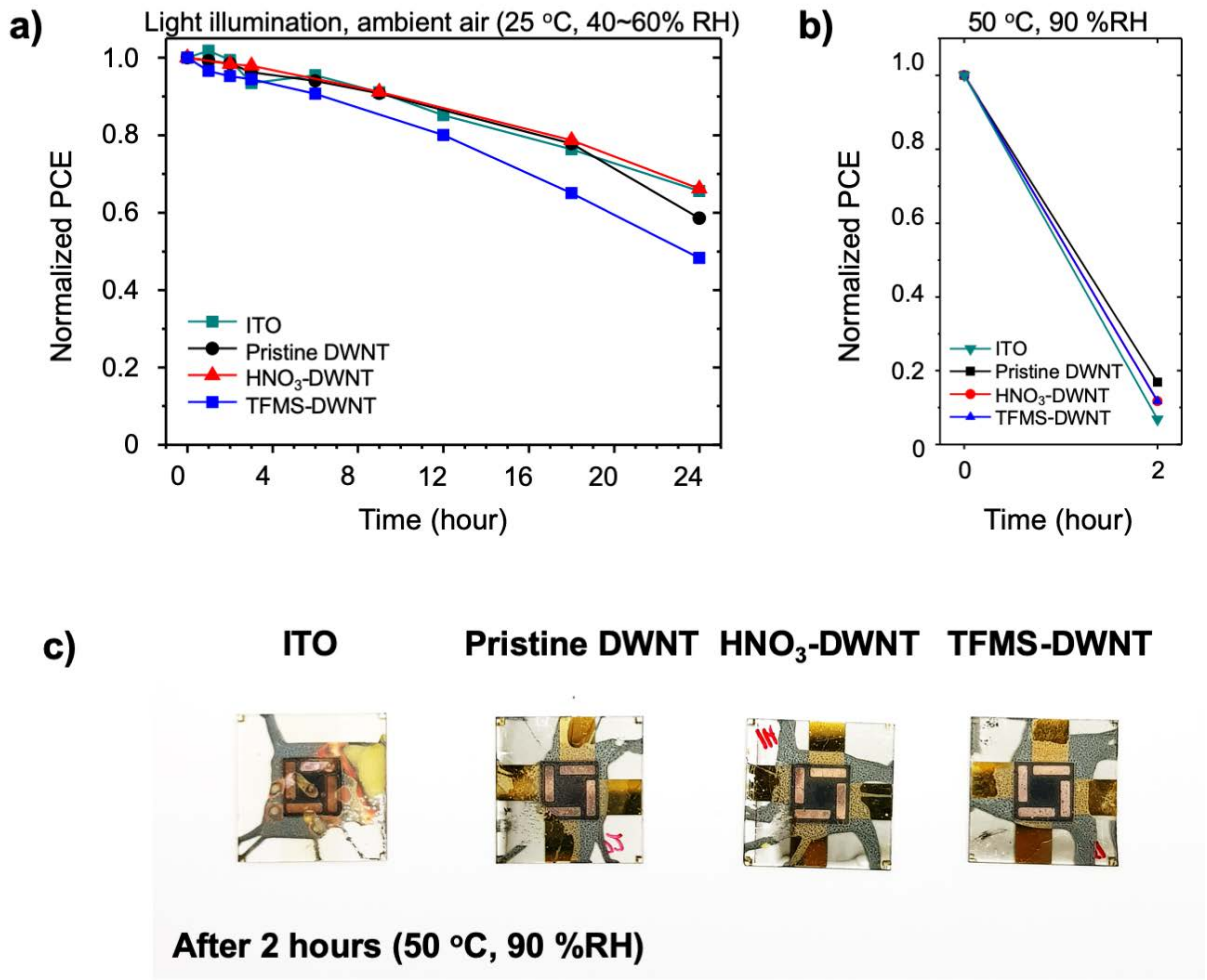

Figure S15. Time evolution of normalized PCE for the ITO-, pristine DWNT-, HNO_3-DWNT-, and TFMS-DWNT-based PSCs without encapsulation under (a) ambience with continuous AM 1.5G one-sun illumination and (b) a severe condition (50 °C, 90% humidity). c) picture of the devices after the stability test.

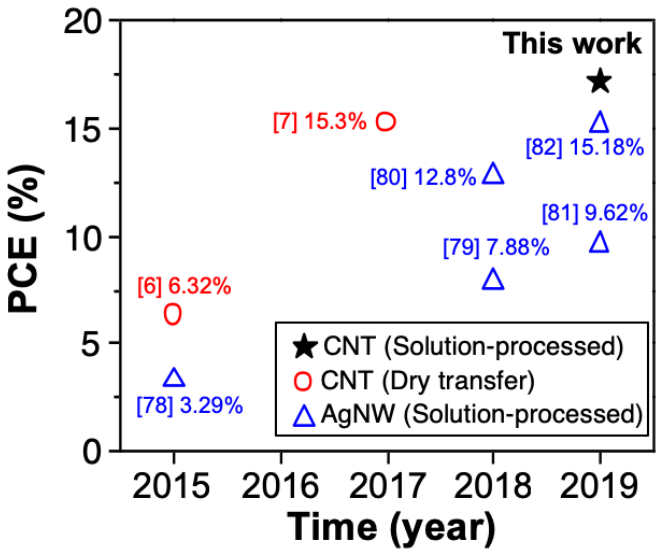

Figure S16. Plot containing the photovoltaic performance of the reported TCO-free PSCs employing CNT and AgNW as a bottom transparent electrode.[6,7,78–82]

Table S7. Table containing the photovoltaic performance and electrode information of the reported TCO-free PSCs employing CNT and AgNW as a bottom transparent electrode.

Year	Bottom Electrode Type	Deposition Technique	PCE (%)	Reference
This work	**TFMS-DWNT**	**Solution (Slot die-coating)**	**17.2**	N/A
2017	HNO_3-SWNT	Dry transfer	15.3	[7]
2015	HNO_3-SWNT	Dry transfer	6.32	[6]
2019	AgNW/RLGO	Solution (Spin-coating)	9.62	[81]
2019	Orthogonal AgNW	Solution (Capillary printing)	15.18	[82]
2018	AgNW/Chi-AsA	Solution	7.88	[79]
2018	a-AZO/AgNW/AZO	Solution (Spin-coating)	12.8	[80]
2015	AgNW/FZO	Solution (Spin-coating) + ALD	3.29	[78]

Table S8. Table containing the photovoltaic performance (including stabilized PCE) and electrode information of the reported PSCs in which CNT was used for bottom and top electrodes.[6,7,12–16, 42, 83–92]

Electrode Type	Year	CNT Type	Deposition Technique	PCE (%)	Stabilized PCE (%)	Reference
Bottom	2019	DWNT	Solution process (Slot-die)	17.2	17.2	This work
	2017	SWNT	Dry transfer	15.3	N/A	[7]
	2015	SWNT	Dry transfer	6.32	N/A	[6]
Top & Bottom	2017	SWNT	Dry transfer	7.32	7.21	[42]
Top	2018	SWNT	Dry transfer	17.56	16.9[a]	[12]
	2018	SWNT	Dry transfer	11.8	N/A	[14]
	2018	CSCNT (MWNT)	Dry transfer	11.9	11.4	[83]
	2017	SWNT/NiO	Screen printing	12.7	N/A	[84]
	2017	CSCNT (MWNT)	Dry transfer	14.3	14	[85]
	2017	SWNT	Dry transfer	17	N/A	[13]
	2017	MWNT	Spin coating	15.23	14.1	[86]
	2017	SWNT	Dry transfer	15	14.3	[16]
	2016	SWNT	Dry transfer	15.5	N/A	[15]
	2016	CSCNT (MWNT)	Dry transfer	10.54	10.385	[87]
	2015	SWNT	Dry transfer	14.7	N/A	[88]
	2015	MWNT	Solution process (Spin coating)	12.67	N/A	[89]
	2015	Twisted MWNT fiber	Fiber spinning	3.03	N/A	[90]
	2014	SWNT and DWNT	Dry transfer	8.31	N/A	[91]
	2014	SWNT and DWNT	Dry transfer	9.9	N/A	[92]

[a]: Stabilized efficiency was obtained by contacting and requesting the corresponding authors.